Title: (limited to 150 characters including spaces)

All-optical reporting of chloride ion driving force in the nervous system.

Authors:

Joshua S. Selfe[1,2], Teresa J. S. Steyn[1,2], Eran F. Shorer[1,2], Richard J. Burman[4], Kira M. Düsterwald[1,2], Ahmed S. Abdelfattah[5,6], Eric R. Schreiter[7], Sarah E. Newey[4], Colin J. Akerman[4], Joseph V. Raimondo[1,2,3]

Affiliations:

[1]Division of Cell Biology, Department of Human Biology, University of Cape Town, South Africa

[2]Neuroscience Institute, University of Cape Town, South Africa

[3]Wellcome Centre for Infectious Disease Research in Africa, Institute of Infectious Disease and Molecular Medicine, University of Cape Town, Cape Town, South Africa.

[4]Department of Pharmacology, University of Oxford, United Kingdom

[5]Department of Neuroscience, Brown University, Providence, RI, USA

[6]Carney Institute for Brain Science, Brown University, Providence, RI, USA

[7]Janelia Research Campus, Howard Hughes Medical Institute, Ashburn, VA, USA

Author correspondence:

JVR (joseph.raimondo@uct.ac.za)

Word count: 4366

Abstract:

Ionic driving forces provide the net electromotive force for ion movement across membranes and are therefore a fundamental property of all cells. In the nervous system, chloride driving force (DF_{Cl}) determines inhibitory signaling, as fast synaptic inhibition is mediated by chloride-permeable $GABA_A$ and glycine receptors. Here we present a new tool for all-Optical Reporting of CHloride Ion Driving force (ORCHID). We demonstrate ORCHID's ability to provide accurate, high-throughput measurements of resting and dynamic DF_{Cl} from genetically targeted cell types over a range of timescales. ORCHID confirms theoretical predictions about the biophysical mechanisms that establish DF_{Cl}, reveals novel differences in DF_{Cl} between neurons and astrocytes under different network conditions, and affords the first *in vivo* measurements of intact DF_{Cl} in mouse cortical neurons. This work extends our understanding of chloride homeostasis and inhibitory synaptic transmission and establishes a precedent for utilizing all-optical methods to assess ionic driving force.

Introduction:

The driving force for chloride (DF_{Cl}) represents the net electromotive force for Cl^- flux across a cell's membrane. DF_{Cl} therefore constitutes the energy per unit charge that is available to mediate a host of fundamental cellular processes[1]. The magnitude of DF_{Cl} indicates how far the electrochemical equilibrium for Cl^- (or Cl^- reversal potential, E_{Cl}) is from the membrane potential (V_m). E_{Cl} is determined by the transmembrane concentration gradient for chloride (Cl^-), which together with V_m sets DF_{Cl} ($DF_{Cl} = V_m - E_{Cl}$). If Cl^- is in electrochemical equilibrium across the membrane (passively distributed), DF_{Cl} has a value of zero. In the nervous system, fast synaptic inhibition is mediated by type A γ-aminobutyric acid receptors ($GABA_A$Rs) and glycine receptors (GlyRs), which are predominantly permeable to Cl^{-2}. As a result, DF_{Cl}, provides the force for Cl^- flux across $GABA_A$Rs and is a principal factor in determining the properties of inhibitory signaling in neuronal networks.

Intracellular Cl^- concentration ($[Cl^-]_i$), is a dynamic variable that is known to differ between subcellular compartments, cell types, and over a range of timescales and network states[3]. Owing to the fact that E_{Cl} is typically close to V_m, relatively small changes to $[Cl^-]_i$ or V_m can have a large effect on the polarity and magnitude of DF_{Cl}, and thus on the effect of inhibitory signalling[4]. Alterations to neuronal DF_{Cl} have been implicated in multiple neurological diseases including epilepsy, chronic pain, schizophrenia, and autism[5–8]. Similarly, DF_{Cl} is thought to be modulated during brain development as part of the GABAergic system's contribution to neural circuit formation[9]. In regions of the mature nervous system, it is believed that DF_{Cl} varies diurnally and is regulated as a function of wakefulness in neurons[10,11] and astrocytes[12]. Therefore, given the central importance of DF_{Cl} for both brain function and dysfunction, techniques for estimating DF_{Cl} are of considerable interest to the neuroscience field.

The most widely used electrophysiological strategy for estimating DF_{Cl} is gramicidin-perforated patch clamp recording[13]. This technique provides electrical access to a target cell of interest without directly disturbing $[Cl^-]_i$. When combined with a means of generating Cl^- selective conductances, such as activation of $GABA_A$Rs or light-sensitive Cl^- channels[14], E_{Cl}, $[Cl^-]_i$, and DF_{Cl} can be estimated. However, gramicidin recordings are technically challenging, have a low success rate and throughput, and have the potential to perturb the intracellular levels of other ions such as K^+ and Na^+, which can indirectly change DF_{Cl} via the action of cation-Cl^- cotransporters (CCCs) such as KCC2 and NKCC1[1]. Meanwhile, the best optical strategies for $[Cl^-]_i$ estimation include fluorescence lifetime imaging (FLIM) of the Cl^--sensitive dye MQAE[15,16] and genetically encoded Cl^- indicators[17]. Ratiometric genetically encoded Cl^- indicators allow for high-throughput measurements and can be targeted to different cell types, although there are challenges associated with ion selectivity, signal-to-noise ratio, and

measurements in intact systems[18–21]. More fundamentally however, whilst currently available optical strategies can provide an estimate of $[Cl^-]_i$, they do not incorporate information about the cell's V_m, and therefore cannot inherently quantify the force available in the transmembrane gradient for Cl^-, which is DF_{Cl}.

Here we present a new approach for easy-to-use, genetically encoded optical estimation of a cell's undisturbed DF_{Cl}, which we term all-Optical Reporting of CHloride Ion Drive (ORCHID). ORCHID has been designed to incorporate the chemi-genetically encoded voltage indicator (GEVI), Voltron2-ST[22], with an independent means of generating Cl^- currents by using light activation of *Guillardia theta* anion channelrhodopsin 2 (GtACR2)[23]. Voltron2-ST is used to measure the magnitude and direction of Cl^--current-induced changes to V_m, thereby providing an estimate of DF_{Cl}. As GtACR2 anion permeability follows the lyotropic series characteristic of other Cl^- channels, including $GABA_A$Rs and GlyRs[23–25], ORCHID could also be considered a reporter of inhibitory receptor driving forces[26,27]. We initially validate the ORCHID approach in mice by demonstrating that it replicates estimates of DF_{Cl} that rely upon the activation of endogenous Cl^- conductances. ORCHID is shown to provide reliable measurements of resting and dynamic DF_{Cl} in different genetically targeted cell populations and across a timescale of seconds and hours. ORCHID is also shown to confirm theoretical predictions regarding the biophysical mechanisms that establish the transmembrane DF_{Cl}. Finally, we use ORCHID to reveal novel cell-type-specific differences in activity-dependent DF_{Cl} changes during periods of network activity, and to provide the first *in vivo* measurements of intact DF_{Cl} in mouse cortical neurons. Together, our results demonstrate that ORCHID allows high-throughput, dynamic estimation of DF_{Cl} in a cell-type-specific manner. This will assist in the study of Cl^- homeostasis and inhibitory synaptic transmission in the nervous system, and establishes a precedent for using all-optical methods to assess ionic driving force more generally.

Results:

ORCHID provides an optical estimate of the magnitude and direction of chloride ion driving force

In order to optically measure DF_{Cl}, we designed a strategy based on combining a genetically encoded optical reporter of V_m, with the simultaneous activation of a light-sensitive transmembrane Cl^- channel (**Fig. 1a-b**). The resulting ORCHID strategy utilizes the recently developed soma-targeted GEVI Voltron2 (Voltron2-ST), and the light-activated Cl^- channel GtACR2, separated via a P2A linker sequence (**Fig. 1c**). The ORCHID construct has a double-floxed design for targeting Cre-expressing cells and is under the control of the EF1α promoter (see **Supplementary Fig. 1** for construct design). Cre-expressing neurons in mouse

hippocampal organotypic brain slices were successfully transduced with adeno-associated virus (AAV) vectors encoding ORCHID (see **Methods**). Prior to imaging, a dye incubation step results in Voltron2-ST protein being irreversibly bound by one of several possible Janelia Fluor (JF) dyes, each of which has different spectral properties[28].

For ORCHID to work, it is critical to achieve spectral separation of the voltage readout using Voltron2-ST from the manipulation of Cl^- currents using GtACR2. Whole-cell patch-clamp recordings from hippocampal pyramidal neurons expressing GtACR2 revealed a wide activation spectrum, with currents being generated by blue (475/28 nm), green (555/28 nm), and yellow (575/25 nm) excitation wavelengths, but not by orange (599/13 nm) or red (635/22 nm) wavelengths (**Fig. 1d**). We therefore utilized JF_{608} together with orange (599/13 nm) excitation light to ensure that GEVI imaging elicited no GtACR2 currents (**Fig. 1e**). Activation of GtACR2 with blue light (475/28 nm) does not significantly excite JF_{608} fluorescence[29]; nonetheless, blue light delivery was rapidly interleaved with camera acquisition to ensure that blue-light-generated autofluorescence would not cause artefacts in the orange GEVI imaging channel (see **Methods**). Imaging neurons expressing only Voltron2-ST labelled with JF_{608} ($Voltron2_{608}$-ST) confirmed that there was no change in fluorescence during blue light delivery (**Fig. 1f**), and whole-cell patch-clamp recordings from ORCHID-expressing neurons confirmed that $Voltron2_{608}$-ST reports linear fluorescence changes in response to voltage steps, thereby establishing that $\Delta F/F_0$ can be used to estimate changes in voltage (ΔV) in subsequent analyses (**Fig. 1g-j**). In ORCHID-expressing neurons, blue light stimulation elicited clear and reproducible V_m shifts, the polarity and magnitude of which could be used to estimate DF_{Cl}, and which showed excellent reproducibility within the same neuron (**Fig. 1k-l**).

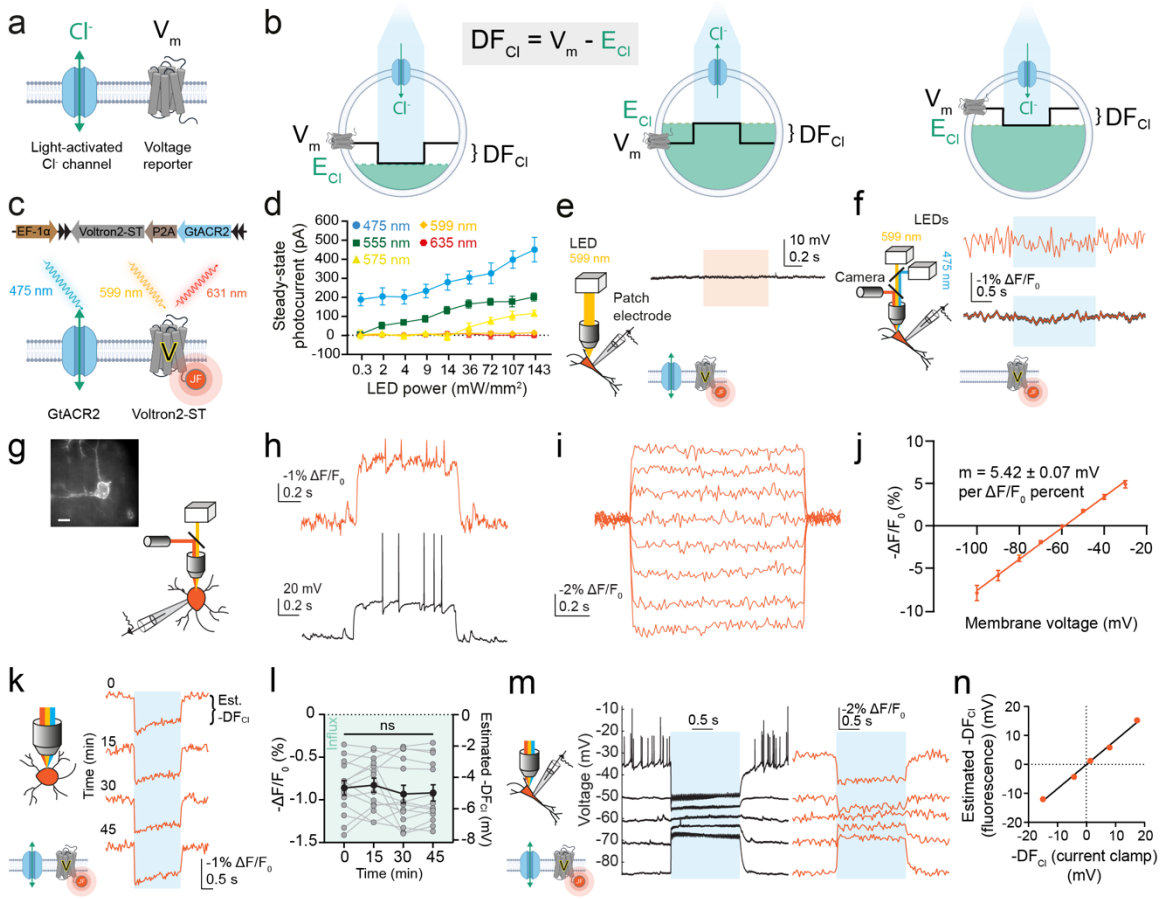

Figure 1: *ORCHID provides an optical estimate of the magnitude and direction of chloride ion driving force.* **a**, Conceptual design of an all-optical strategy to estimate DF_{Cl}, combining a light-activated Cl^- channel with an optical voltage reporter. **b**, Activation of a Cl^- conductance (blue) drives V_m (black trace) toward E_{Cl} (green dotted line). The V_m shift from before to after Cl^- channel activation provides an estimate of DF_{Cl} ($DF_{Cl} = V_m - E_{Cl}$). Left, E_{Cl} is negative with respect to initial V_m, constituting a driving force that results in Cl^- influx and hyperpolarization. Middle, due to higher $[Cl^-]_i$ (green shading), E_{Cl} is positive with respect to initial V_m, and DF_{Cl} now causes Cl^- efflux and depolarization. Right, despite identical E_{Cl}, initial V_m results in DF_{Cl} that causes influx and hyperpolarization. **c**, Top, components of the ORCHID construct. Bottom, ORCHID utilizes co-expression of GtACR2 with Voltron2-ST. Blue light (475/28 nm) activation of GtACR2 evokes a conductance that is predominantly mediated by Cl^- (green arrow). $Voltron2_{608}$-ST is excited by orange light (599/13 nm) and emits red fluorescence (631 nm peak emission) that is sensitive to V_m. **d**, GtACR2 activation spectrum; steady-state photocurrents generated by LED light of different peak wavelengths at different intensities in hippocampal neurons expressing GtACR2 during whole-cell patch-clamp recordings. **e**, Current-clamp recording from a neuron virally transfected with ORCHID confirms illumination with the 599/13 nm LED (orange rectangle) does not change V_m. **f**, Voltage imaging of a hippocampal neuron virally transduced with $Voltron2_{608}$-ST alone (no GtACR2) reveals that blue light delivery, by strobing the blue LED in between camera exposures, causes no change in measured fluorescence (top, orange trace); averaged recorded fluorescence from 29 neurons showing mean ± standard error of the mean (SEM; bottom, orange trace and grey shading respectively). **g**, Setup for patch-clamp characterization of $Voltron2_{608}$-ST in a hippocampal neuron. Inset: widefield fluorescence image of the neuron patched in 'h'; scale bar: 10 µm. **h**, Current-clamp recording (black trace) and the $Voltron2_{608}$-ST fluorescence response (orange trace) following a 200 pA current injection. **i**, $Voltron2_{608}$-ST fluorescence response to 10 mV voltage steps (V_{hold} = -60 mV). **j**, Voltage-fluorescence relationship of $Voltron2_{608}$-ST, with a slope 5.42 ± 0.07 mV per $\Delta F/F_0$ percent (R^2 = 0.9311, n = 7). **k**, Activation of GtACR2 as part of ORCHID with a 475/28 nm LED (schematic on left and blue rectangle) evoked fluorescence transients from imaged $Voltron2_{608}$-ST (orange traces), which reflected DF_{Cl} and were stable over 45 min. **l**, Population data showing that estimates of DF_{Cl} made using ORCHID remained stable (repeated measures one-way ANOVA, P = 0.2469, n = 12). Green shading indicates direction of estimated anion flux. **m**, ORCHID was used to estimate DF_{Cl} in neurons current clamped at a range of V_m values (left panel, V_m; right panel, fluorescence). Action potentials are truncated due to averaging (**Methods**). **n**, The fluorescence-voltage relationship of $Voltron2_{608}$-ST (j) was used to convert $\Delta F/F_0$ measurements at each V_m to estimated DF_{Cl} values. These were equivalent to the DF_{Cl} values recorded at each V_m using the current-clamp recording (R^2 = 0.9955). ns = not significant (P > 0.05); error bars indicate mean ± SEM.

125

126 To assess ORCHID's ability to quantify DF_{Cl}, we performed current-clamp recordings during
127 voltage imaging in ORCHID-expressing neurons. Different DF_{Cl} values were imposed by
128 injecting current via the patch pipette, whilst performing voltage imaging and generating Cl^-
129 currents via blue-light activation of ORCHID (**Fig. 1m-n**). The relationship between $\Delta F/F_0$ and
130 ΔV (**Fig. 1j**) was used to convert the measured $\Delta F/F_0$ values into estimations of Cl^--current-
131 induced changes to V_m; these optically determined DF_{Cl} values were found to be equivalent to
132 DF_{Cl} measured from the simultaneous current-clamp recordings (**Fig. 1n**; R^2 = 0.9955). This
133 demonstrated that the ability of ORCHID to estimate DF_{Cl} is as accurate as using current-
134 clamp recordings, with both methods accurately determining the direction of DF_{Cl} and inclined
135 to underestimate the full magnitude of DF_{Cl}. ORCHID's ability to detect a change in DF_{Cl} was
136 further confirmed by comparing measurements of DF_{Cl} made before and after a neuron
137 experienced an increase in $[Cl^-]_i$ imposed by dialysis (**Supplementary Fig. 2**).

138 As further validation, we assessed ORCHID's ability to accurately determine DF_{Cl} when the
139 Cl^- currents were generated by activating endogenous Cl^--permeable channels in different
140 neuronal populations. Transgenic mice expressing Cre recombinase in different cell types
141 were used to restrict reporter expression to either CaMKIIα+ pyramidal neurons or GAD2+
142 interneurons. Voltron2-ST labelled with JF_{549} ($Voltron2_{549}$-ST) was used to assess DF_{Cl} via
143 endogenous $GABA_A$Rs on the cell soma, which were activated by picolitre delivery of GABA
144 (500 μM) via a glass micropipette and in the presence of a $GABA_B$R antagonist (5 μM CGP-
145 55845). We found this to be an effective method of estimating DF_{Cl} (**Supplementary Fig. 3, 4**
146 **and 5**) and revealed that both CaMKIIα+ pyramidal neurons and GAD2+ interneurons exhibit
147 hyperpolarizing $GABA_A$R-driven DF_{Cl} under these conditions, with GAD2+ interneurons
148 exhibiting slightly greater DF_{Cl} (**Fig. 2a-c**). When these experiments were conducted using
149 ORCHID, our all-optical strategy revealed similar hyperpolarizing DF_{Cl} values for both
150 neuronal populations, again with slightly greater DF_{Cl} in GAD2+ interneurons compared to
151 CaMKIIα+ pyramidal neurons (**Fig. 2d-f**).

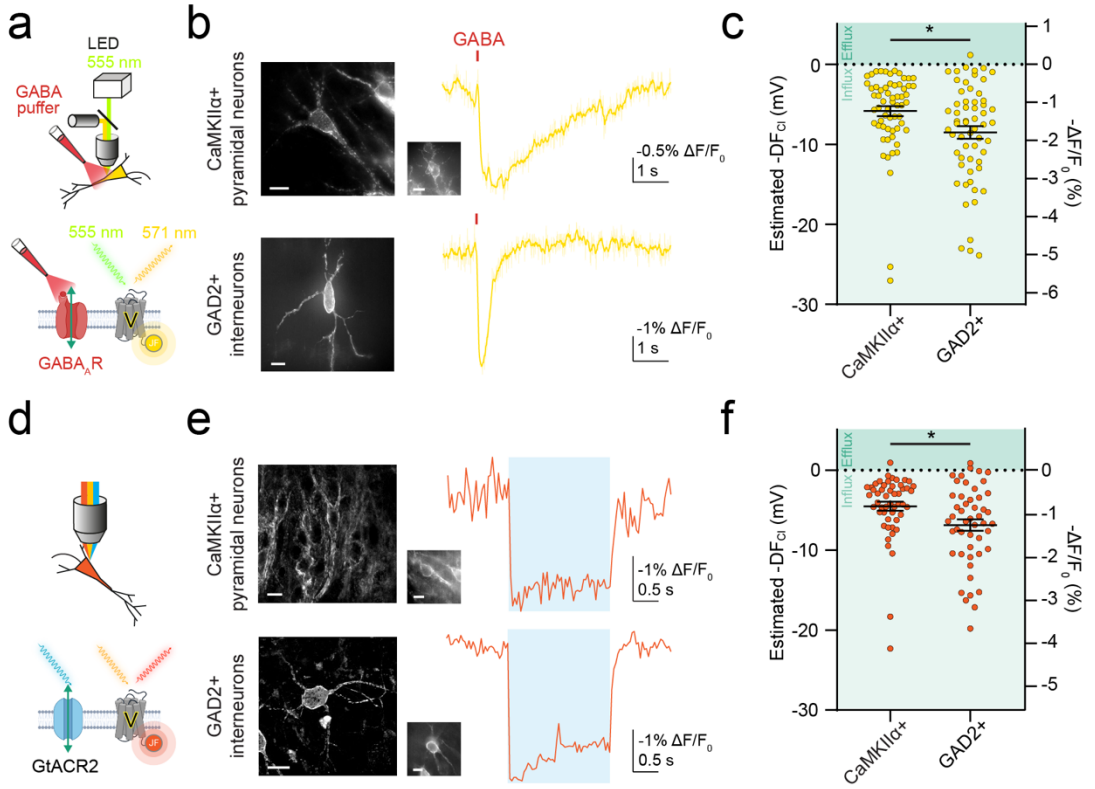

Figure 2: *ORCHID reports endogenous chloride ion driving force in different neuronal populations.* **a**, Schematics demonstrating imaging of Voltron2$_{549}$-ST together with activation of endogenously expressed GABA$_A$Rs through picolitre delivery of GABA (red; 500 µM) directed at the cell soma to estimate DF$_{Cl}$. CGP-55845 (5 µM) was used to block GABA$_B$Rs. **b**, Widefield fluorescence images of CaMKIIα+ pyramidal neurons (top) and GAD2+ interneurons (bottom) expressing Voltron2$_{549}$-ST (left) and fluorescence recordings used to estimate DF$_{Cl}$ from each cell type (right, yellow traces), with the cells that were recorded from shown inset if not in the main image; scale bar: 10 µm. Red bar indicates GABA application. **c**, Population data showing estimated DF$_{Cl}$ was different between cell types (CaMKIIα+: -5.85 ± 0.62 mV vs GAD2+: -8.52 ± 0.79 mV, Mann-Whitney test, P = 0.0068, n = 62 and 60 cells respectively). **d**, Schematics depicting ORCHID's use for estimating DF$_{Cl}$ in neurons. **e**, Left, confocal images of CaMKIIα+ pyramidal neurons (top) and GAD2+ interneurons (bottom) expressing ORCHID in mouse organotypic hippocampal brain slices. Right, fluorescence recordings used to estimate DF$_{Cl}$ from each cell type, with widefield image of the cell recorded from (inset); scale bar: 10 µm. **f**, Estimated DF$_{Cl}$ was significantly different between cell types (CaMKIIα+: -4.52 ± 0.57 mV vs GAD2+: -6.88 ± 0.72 mV, Mann-Whitney test, P = 0.0057, n = 51 and 49 cells respectively). ns = not significant (P > 0.05); *P ≤ 0.05; error bars indicate mean ± SEM.

ORCHID strategies confirm theoretical predictions regarding chloride ion driving force

The accepted view is that DF$_{Cl}$ is established by the action of CCCs such as KCC2 and NKCC1, which are able to use secondary active transport to move Cl^- against its transmembrane concentration gradient by utilizing cation gradients established by the primary active transporter, Na^+/K^+-ATPase[1]. However, work using the genetically encoded Cl^- indicator, Clomeleon, challenged this idea by proposing that impermeant anions (and not CCCs) set $[Cl^-]_i$ and DF$_{Cl}$[30]. We sought to examine these biophysical principles by first using a theoretical model to make predictions about the mechanisms that establish DF$_{Cl}$, and then using ORCHID strategies to assess these predictions. We extended a computational

178 biophysical model of a single neuron based on the pump-leak mechanism that incorporated
179 the permeant ions (Na^+, K^+, Cl^-, HCO_3^-) and their movement via leak channels and receptors,
180 the Na^+/K^+- ATPase, and the major Cl^- extruder in mature neurons, KCC2. The model also
181 incorporated impermeant anions X with average charge z[31], pH control via the HCO_3^--buffering
182 system and Na^+/H^+ exchange, dynamic volume, water permeability, and synaptic $GABA_A$Rs
183 that were able to elicit Cl^- conductances and resulting changes in V_m (**Fig. 3a**). As expected,
184 simulating a block of KCC2 in the model caused a positive shift in both E_{Cl}, E_{GABAA} and $[Cl^-]_i$,
185 with a small effect on V_m, (**Fig. 3b**). This resulted in a substantial shift in DF_{Cl} causing a
186 decrease in amplitude and an inversion in polarity of $GABA_A$R-mediated potentials (**Fig. 3c**).
187 Meanwhile, simulating the addition of impermeant anions by reducing their average charge z
188 generated a persistent negative shift in E_{Cl}, E_{GABAA} and $[Cl^-]_i$, consistent with previous
189 observations[31]. However, this manipulation caused ionic redistribution such that V_m also
190 shifted and in a manner proportional to the effects upon E_{Cl} and E_{GABAA} (**Fig. 3d)**. Therefore
191 $GABA_A$R-mediated potentials were of a similar size following the addition of impermeant
192 anions (**Fig. 3e**).

193 To empirically test these predictions, we used ORCHID strategies to measure the effect of
194 manipulations upon DF_{Cl} in hippocampal pyramidal neurons. First, we observed that addition
195 of the selective inhibitor of KCC2, VU0463271 (VU; 10 μM), caused a robust depolarizing shift
196 in estimated DF_{Cl} (**Fig. 3f-i**). This was evident when DF_{Cl} was measured via activation of
197 $GABA_A$Rs or all-optically, and the effect upon DF_{Cl} reversed following washout of VU (**Fig. 3f-**
198 **i**). Second, we assessed DF_{Cl} before and after the addition of intracellular impermeant anions,
199 which was achieved by single-cell electroporation of fluorescently tagged anionic dextrans
200 (Alexa Fluor 488, see **Methods**) (**Fig. 3j**). Successful addition of impermeant anions was
201 confirmed by directly observing the fluorescent dextrans within the neuron of interest, and DF_{Cl}
202 was estimated from the size and polarity of $GABA_A$R responses before and after the
203 electroporation procedure (**Fig. 3k-l**). Consistent with the prediction of the modelling work, this
204 revealed that the addition of impermeant anions had no detectable effect upon DF_{Cl} (**Fig. 3m**).
205 Therefore, ORCHID strategies are able to confirm theoretical predictions about the
206 mechanisms that establish DF_{Cl}.

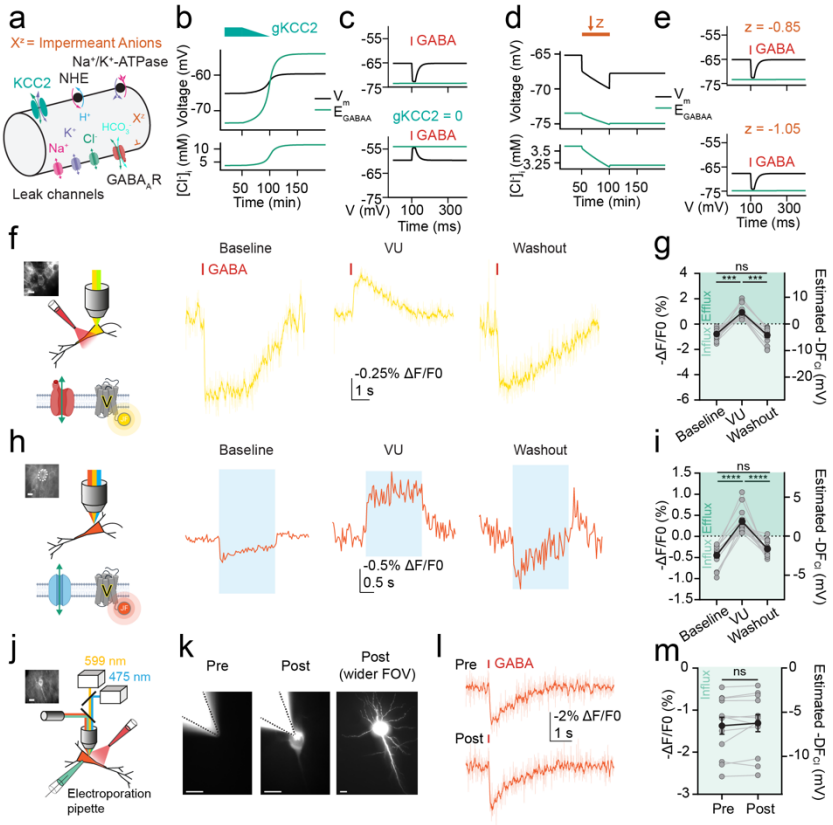

Figure 3: *ORCHID strategies confirm theoretical predictions regarding chloride ion driving force* **a**, Biophysical computational model of ion dynamics based on the pump-leak mechanism consisted of a single cylindrical compartment (1 µm diameter; 25 µm length) within an extracellular environment that had fixed ion concentrations. Transmembrane movement of permeant ions (Na^+, K^+, Cl^-, HCO_3^-) was modelled though leak channels, KCC2, Na^+/K^+-ATPase, and $GABA_AR$. Impermeant anions, X, with average charge z could not cross the membrane and were present in both intracellular and extracellular environments. pH regulation was implemented via the HCO_3^--buffer system and Na^+/H^+ exchange. **b**, Top, simulated decrease in gKCC2 from 120 µS/cm² to 0 µS/cm² between 50 min and 100 min (teal bar) caused an increase in E_{GABAA} (green) and smaller changes in V_m (black). Bottom, increased $[Cl^-]_i$ in response to reduced gKCC2. **c**, Simulated synaptic $GABA_AR$ activation (red bar) in the neuron causes hyperpolarization with KCC2 intact (top), but depolarization with KCC2 blocked (bottom), indicating a shift from a hyperpolarizing to depolarizing driving force. **d,** As in 'b' but with average intracellular impermeant anion charge (z) shifted from -0.85 to -1.05 between 50 min and 100 min (orange bar). Top, proportional drop in V_m (black) and E_{GABAA} (green) reflected a relatively unchanged DF_{Cl} despite altered z. Bottom, reduced $[Cl^-]_i$ in response to decreased z. **e**, Simulated synaptic $GABA_AR$ activation results in similarly sized hyperpolarization in the neuron with default z of -0.85 (top), and with reduced z of -1.05 (bottom). **f**, Estimated DF_{Cl} recorded in CaMKIIα+ pyramidal neurons using activation of endogenous $GABA_ARs$ and $Voltron2_{549}$-ST at baseline (left), during KCC2 blockade by VU (middle; 10 µM), and after VU washout (right). Inset: widefield fluorescence image of the CaMKIIα+ pyramidal neuron from which the recording was made; scale bar: 10 µm. **g**, Population data showing blockade of KCC2 by VU caused a significant depolarization of DF_{Cl} in CaMKIIα+ neurons (left, Wilcoxon matched-pairs signed rank tests, wash-in $P = 0.0001$, washout $P = 0.0001$, $n = 14$, baseline vs washout comparison, $P = 0.6698$). Green shading indicates direction of estimated anion flux. **h**, All-optical ORCHID was used to record DF_{Cl} as in 'f'. **i**, Population data showing VU caused a significant shift in DF_{Cl} recorded using ORCHID in both CaMKIIα+ pyramidal neurons (left, Wilcoxon matched-pairs signed rank tests, wash-in $P < 0.0001$, washout $P < 0.0001$, $n = 16$, baseline vs washout comparison, $P = 0.1046$). **j**, Schematic of experimental setup for electroporation of CaMKIIα+ pyramidal neurons with fluorescently tagged (Alexa Fluor 488) anionic dextrans. Inset: widefield fluorescence image of $Voltron2_{608}$-ST fluorescence of targeted neuron; scale bar: 10 µm. **k**, Successful electroporation of neurons with anionic dextrans was verified by observing Alexa Fluor 488 fluorescence restricted to the cell of interest; scale bars: 10 µm. **l**, Activation of endogenous $GABA_ARs$ during $Voltron2_{608}$-ST voltage imaging was used to estimate DF_{Cl} from the pyramidal neuron in 'j' and 'k', both pre-electroporation (pre) and post-electroporation (post). **m**, Population data showing that the addition of impermeant anions had no observable effect on estimated DF_{Cl} (paired t-test, $P = 0.2506$, $n = 12$). ns = not significant ($P > 0.05$); *$P \leq 0.05$; ***$P \leq 0.001$; ****$P \leq 0.0001$; error bars indicate mean ± SEM.

242

243 **ORCHID reveals dynamic chloride ion driving forces over different timescales**

244 In neurons, $[Cl^-]_i$ and E_{Cl} are considered dynamic variables under the control of multiple
245 activity-dependent processes, and are thought to vary over a range of timescales[3]. We
246 therefore sought to use ORCHID to investigate DF_{Cl} dynamics over different timescales, and
247 first examined periods of elevated network activity where intense activation of $GABA_ARs$ is
248 hypothesized to cause transient changes in DF_{Cl}[4]. ORCHID was expressed in CaMKIIα+
249 pyramidal neurons or GAD2+ interneurons, and we used low-Mg^{2+} artificial cerebrospinal fluid
250 (aCSF) to induce seizure-like events (SLEs) in mouse organotypic hippocampal brain slices.
251 DF_{Cl} was estimated using ORCHID in target cells, whilst a simultaneous whole-cell current-
252 clamp recording from a nearby CA1/3 pyramidal neuron provided an independent readout of
253 network activity (**Fig. 4a-d**). The SLEs were characterized by pronounced depolarizing shifts
254 in V_m and intense firing of action potentials, which could be observed both in the current-clamp
255 recordings and in ORCHID's voltage signals (**Fig. 4a,c**). CaMKIIα+ pyramidal neurons showed
256 substantial activity-dependent changes in DF_{Cl}, exhibiting shifts in polarity from a
257 hyperpolarizing DF_{Cl} at baseline to a depolarizing DF_{Cl} immediately post-SLE, which returned
258 to a hyperpolarizing DF_{Cl} > 2 min after the SLE (**Fig. 4b**). Similarly, GAD2+ interneurons
259 exhibited a hyperpolarizing DF_{Cl} at baseline that flipped polarity to become a depolarizing DF_{Cl}
260 immediately post-SLE, and subsequently returned to a hyperpolarizing DF_{Cl} after > 2 min (**Fig.**
261 **4d**). These dynamics were confirmed by using endogenous $GABA_AR$ activation to estimate
262 DF_{Cl} in CaMKIIα+ pyramidal neurons and GAD2+ interneurons (**Supplementary Fig. 6**).
263 Furthermore, shifts in DF_{Cl} have been postulated to occur immediately prior to seizure onset
264 and to form part of the mechanism by which seizures initiate[32]. In line with this, ORCHID
265 detected more modest decreases in the magnitude of DF_{Cl} between baseline and immediately
266 prior to the SLE (< 5 s prior to SLE onset) in both CaMKIIα+ pyramidal neurons and GAD2+
267 interneurons (**Fig. 4b,d**), suggesting that DF_{Cl} begins to break down before SLE onset.

268 Having demonstrated ORCHID's ability to report DF_{Cl} dynamics on a timescale of seconds,
269 we next sought to assess ORCHID's potential to measure longer-term changes in a neuron's
270 DF_{Cl}, such as those that have been linked to activity-dependent changes in CCCs[33]. To this
271 end, ORCHID was used to track DF_{Cl} in the same GAD2+ interneurons before and after a 180
272 min treatment with either 4-aminopyridine (4-AP; 50 μM) to increase neuronal activity or
273 tetrodotoxin (TTX; 1 μM) to silence neuronal activity (**Fig. 4e**). When DF_{Cl} measurements were
274 made after the 180 min treatment and a subsequent 10 min incubation in TTX, ORCHID
275 revealed that raising neuronal activity had caused a sustained and robust depolarizing shift in
276 neuronal DF_{Cl} (**Fig. 4f,g**), which was not evident in neurons that had been silenced with TTX

(**Fig. 4h,i**), or in neurons exposed to vehicle control for the equivalent 180 min period (**Supplementary Fig. 7**). Hence, ORCHID can provide high-throughput measurements of resting and dynamic DF_{Cl} across timescales of seconds and hours.

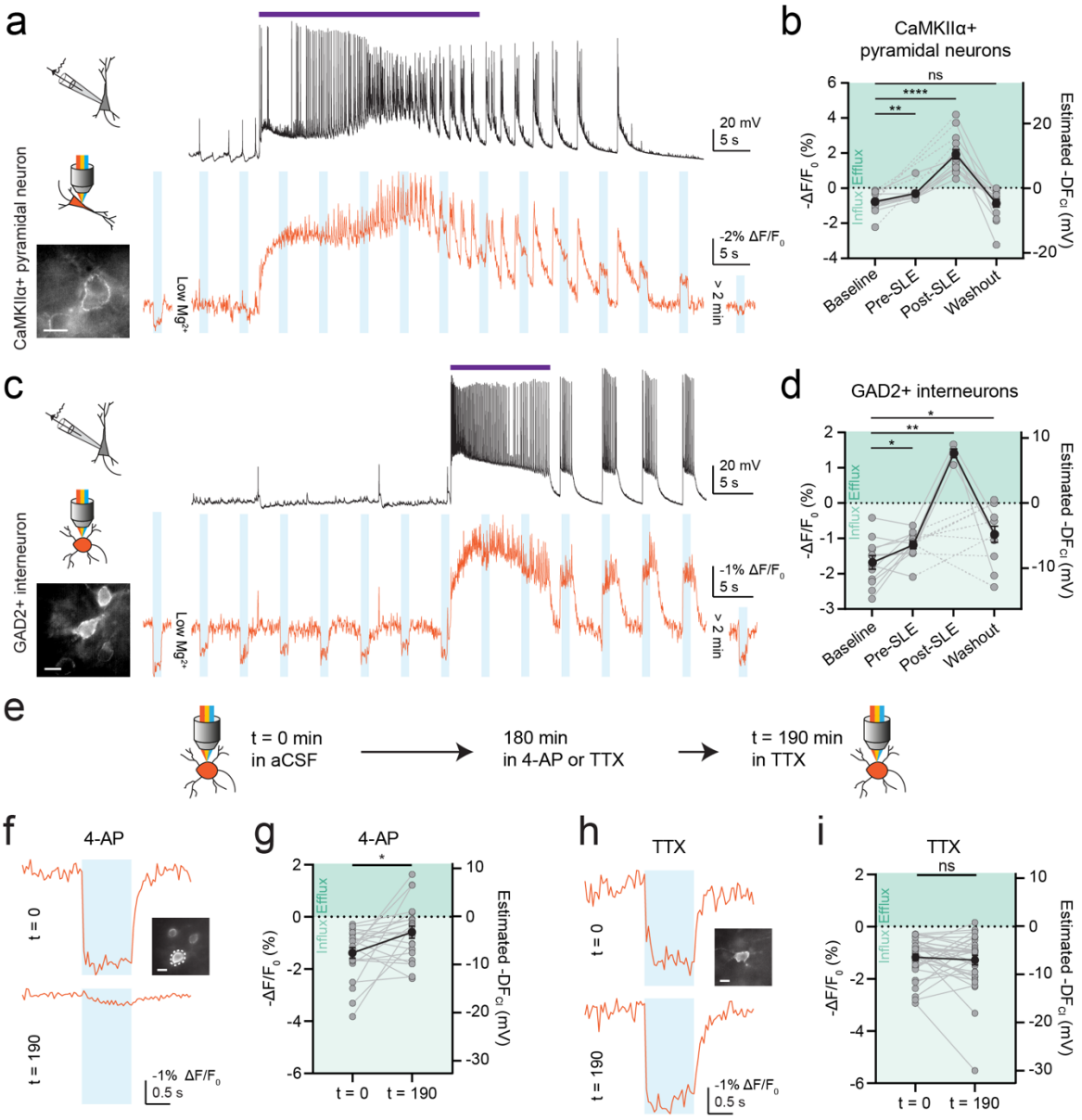

Figure 4: *ORCHID reveals dynamic chloride ion driving forces over different timescales.* **a**, ORCHID was used to investigate activity-dependent variation in DF_{Cl} in CaMKIIα+ pyramidal neurons during low-Mg^{2+} induced SLEs. Top, whole-cell current-clamp recording from a CA1/3 pyramidal neuron provided an independent readout of SLEs (black trace; purple bar indicates SLE). Bottom, concurrent ORCHID recording to measure DF_{Cl} (orange trace). Inset: widefield fluorescence images of recorded cell; scale bar: 10 µm. **b**, Population data from CaMKIIα+ pyramidal neurons comparing DF_{Cl} at baseline, prior to low-Mg^{2+} aCSF wash-in (wash-in labelled as "Low Mg^{2+}" in 'a' and 'c'), immediately pre-SLE (< 5 s before onset), immediately post-SLE (< 20 s after SLE cessation), and > 2 min post-SLE (washout). DF_{Cl} showed a large shift from hyperpolarizing at baseline to depolarizing post-SLE (Wilcoxon matched-pairs signed rank test, $P < 0.0001$, $n = 15$). > 2 min after the SLE (washout), DF_{Cl} had returned to baseline levels (baseline vs washout: Wilcoxon matched-pairs signed rank test, $P = 0.5995$, $n = 15$). Additionally, there was a significant depolarizing shift in DF_{Cl} between the baseline recordings and the recordings made pre-SLE (Wilcoxon matched-pairs signed rank test, $P = 0.0020$, $n = 10$). Dotted lines indicate cells for which pre-SLE DF_{Cl} was not recorded ($n = 5/15$). **c**, As in 'a' but with GAD2+ interneurons targeted for ORCHID recording. **d**, Population data of DF_{Cl} in GAD2+ interneurons showed hyperpolarizing DF_{Cl} at baseline. In 8/12 cells from which recordings were made, stimulation of GtACR2 as part of ORCHID caused slice-wide burst firing after the

occurrence of a SLE, which persisted for minutes. In the 4/12 recordings where GtACR2-induced burst firing did not occur, there was a significant depolarizing shift in DF_{Cl} post-SLE (paired t-test, $P = 0.0047$, $n = 4$); dotted lines indicate cells in which burst-firing occurred and post-SLE DF_{Cl} could not be recorded ($n = 8/12$). When recorded again > 2 min after the SLE, DF_{Cl} had returned to near baseline values (baseline vs washout, paired t-test, $P = 0.0317$, $n = 12$). Additionally, there was a significant depolarizing shift in DF_{Cl} between the baseline recordings and the recordings made pre-SLE (paired t-test, $P = 0.0234$, $n = 12$). **e**, Schematic of experimental design with ORCHID used to make paired recordings of DF_{Cl} 190 min apart in the same GAD2+ interneurons in organotypic hippocampal brain slices. **f**, Top, baseline recording before slice was incubated in 4-AP (50 μM) for 180 min. Bottom, recording after the slice had been transferred to aCSF containing TTX (1 μm) for 10 min. Inset: widefield fluorescence image of recorded neuron; scale bar: 10 μm. **g**, Population data showing DF_{Cl} depolarized significantly after a 180 min incubation in 4-AP (Wilcoxon matched-pairs signed rank test, $P = 0.0229$, $n = 22$). **h**, As in 'f' but with recordings of DF_{Cl} before and after a 190 min incubation in TTX. Inset: widefield fluorescence image of recorded neuron; scale bar: 10 μm. **i**, Population data showing magnitude of DF_{Cl} was not significantly different after a 190 min incubation in TTX (Wilcoxon matched-pairs signed rank test, $P = 0.5888$, $n = 34$). ns = not significant ($P > 0.05$); *$P \leq 0.05$; error bars indicate mean ± SEM.

Astrocytes sustain an outward chloride ion driving force during enhanced network activity

Astrocytes are known to play important roles in regulating and maintaining neuronal ion gradients by modulating extracellular ion concentrations. However, due to the difficulty in performing electrophysiological recordings from this cell type, it has not previously been possible to measure astrocytic DF_{Cl} across different types of network activity. Using the Cre-lox system, we restricted ORCHID expression to GFAP+ astrocytes in mouse organotypic hippocampal brain slices and optically estimated DF_{Cl}. We observed that, in stark contrast to neurons, the astrocytic DF_{Cl} under baseline conditions was strongly depolarizing (**Fig. 5a-c**). A related idea that has been proposed is that astrocytes may serve to continuously supplement Cl^- into the extracellular space during periods of enhanced network activity, and thereby help to maintain the effectiveness of $GABA_AR$-mediated inhibitory synaptic transmission[12]. To test this explicitly, we used ORCHID to continuously monitor astrocytic DF_{Cl} across periods of intense network activity, which was achieved by inducing SLEs through low-Mg^{2+} aCSF. Whilst there was a modest decrease in the magnitude of DF_{Cl} during the SLE, ORCHID revealed that the astrocytes continued to exhibit a strongly depolarizing DF_{Cl} before and after the SLE, and are therefore capable of maintaining a driving force for Cl^- efflux during substantial changes in network activity (**Fig. 5d,e**). When compared to neurons, such markedly different resting and dynamic DF_{Cl} in astrocytes suggests that they differ in how they utilize major Cl^- regulatory mechanisms such as NKCC1 and KCC2, which act to transport Cl^- in and out of the cell respectively. To assess this, we performed single-nucleus RNA sequencing (snRNAseq) and analyzed the transcriptomes of 46509 nuclei from the same hippocampal brain slice preparations (4 samples, 36 brain slices per sample; see **Methods**). Unbiased clustering of the transcriptomic profiles identified 6329 pyramidal neurons and 12355 astrocytes (confirmed by high relative expression of CaMKIIα and GFAP respectively; **Fig. 5f**). After normalizing for total gene expression per nucleus, we then compared the

338 average gene expression for KCC2 (Slc12a5) and NKCC1 (Slc12a2). We observed that KCC2
339 was more highly expressed in pyramidal neurons than astrocytes. Meanwhile NKCC1
340 expression, although comparatively low in both cell types, was higher in astrocytes than
341 pyramidal neurons (**Fig. 5f**). Thus, ORCHID reveals unique features of astrocytic DF_{Cl}
342 compared to neurons, that correlate with differences in their Cl^--transport mechanisms.

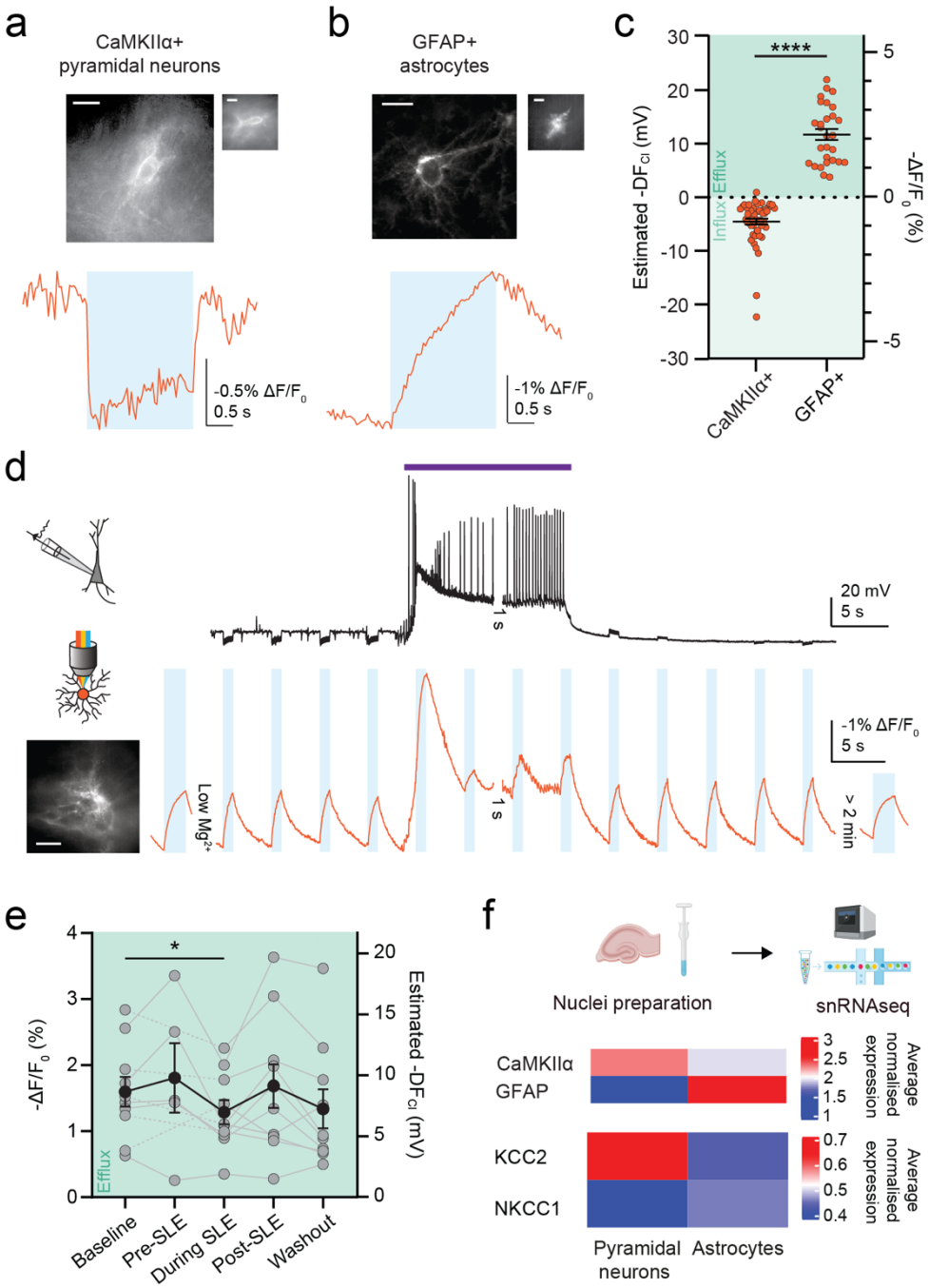

343

344 **Figure 5:** *Astrocytes sustain an outward chloride ion driving force during enhanced network activity.* ORCHID was
345 used to compare DF_{Cl} in CaMKIIα+ pyramidal neurons (**a**) and GFAP+ astrocytes (**b**). Widefield and confocal
346 images of cells expressing ORCHID (top) and fluorescence recordings used to estimate DF_{Cl} from each cell type
347 (bottom), with the cell that was recorded from shown inset; scale bar: 10 µm. **c**, Comparison of estimated DF_{Cl}
348 between CaMKIIα+ pyramidal neurons and GFAP+ astrocytes. Estimated DF_{Cl} in GFAP+ astrocytes was
349 significantly different to estimated DF_{Cl} in CaMKIIα+ pyramidal neurons (CaMKIIα+: -4.52 ± 0.57 mV vs GFAP+:

11.73 ± 1.025 mV; Mann-Whitney test, $P < 0.0001$, $n = 51$ and 28 cells respectively). **d**, ORCHID was used to investigate network activity-dependent variation in DF_{Cl} in GFAP+ astrocytes during low-Mg^{2+} induced elevated network activity and SLEs. Top, a whole-cell current-clamp recording from a CA1/3 pyramidal neuron provided an independent readout of network activity (black trace; purple bar indicates SLE). Bottom, concurrent ORCHID recording to measure DF_{Cl} (orange trace). Inset: widefield fluorescence images of recorded cell; scale bar: 10 µm. **e**, Population data of DF_{Cl} in GFAP+ astrocytes showed depolarizing DF_{Cl} at baseline. This was maintained pre-SLE (paired t-test, $P = 0.3098$, $n = 5$), post-SLE (paired t-test, $P = 0.5813$, $n = 10$), and after washout (Wilcoxon matched-pairs signed rank test, $P = 0.0840$, $n = 10$). However, there was a small decrease in the magnitude of DF_{Cl} during the SLE (baseline vs during SLE: paired t-test, $P = 0.0334$, $n = 10$). Dotted lines indicate cells for which pre-SLE DF_{Cl} was not recorded ($n = 5/10$). **f**, Top, schematic showing nuclear dissociation and snRNAseq from mouse organotypic hippocampal brain slices performed using the 10X Genomics platform. Middle, heatmap showing the average normalized expression of CaMKIIα and GFAP RNA in the pyramidal neuron and astrocyte clusters respectively. Bottom, heatmap showing the average normalized gene expression between pyramidal neurons vs astrocytes, which was different for KCC2 (Slc12a5, $P = 0.0324$, $n = 4$ samples) and NKCC1 (Slc12a2, $P = 0.0087$, $n = 4$ samples). ns = not significant ($P > 0.05$); *$P \leq 0.05$; ****$P \leq 0.0001$; error bars indicate mean ± SEM.

In vivo determination of resting and dynamic chloride ion driving forces in neurons

Finally, ORCHID offers the opportunity to generate estimates of undisturbed DF_{Cl} in the intact brain. We therefore assessed ORCHID's ability to report resting and dynamic DF_{Cl} *in vivo*. ORCHID was expressed in layer 1 (L1) GAD2+ interneurons in the murine primary somatosensory cortex (S1), and anesthetized *in vivo* imaging was combined with simultaneous local-field potential (LFP) recordings to provide an independent measure of local population activity (**Fig. 6a**; **Methods**). Under baseline conditions, we observed a range of DF_{Cl} polarities and magnitudes across different neurons, including hyperpolarizing, shunting, and depolarizing DF_{Cl} (**Fig. 6b,c**). In a subset of mice, we performed continuous DF_{Cl} measurements before and after infusing 4-AP (500 µM) into the cortex to elicit SLEs (**Methods**). The occurrence of SLEs was confirmed from the LFP recordings and DF_{Cl} could be tracked in the same individual neurons before and after the SLE (**Fig. 6d**). This revealed that L1 GAD2+ interneurons exhibit a large depolarizing shift in DF_{Cl} following 4-AP infusion and the occurrence of a SLE (**Fig. 6e**). This demonstrates that *in vivo* ORCHID affords easy and rapid reporting of resting and activity-dependent dynamic shifts in DF_{Cl} in the intact brain, under control and disease-relevant conditions.

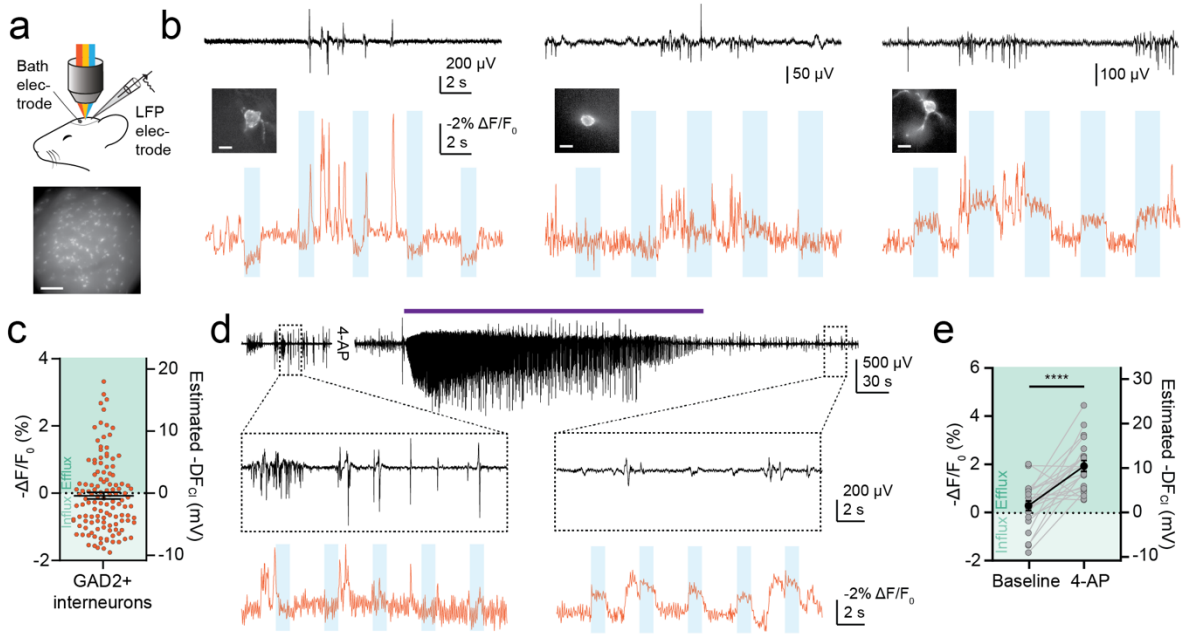

Figure 6: *In vivo determination of resting and dynamic chloride ion driving forces in neurons.* **a**, Schematic of experimental setup (top) and a widefield fluorescence image of a region of L1 in S1 with GAD2+ interneurons expressing ORCHID (bottom); scale bar: 100 µm. **b**, LFP recordings were used to independently record population activity (black traces; top). ORCHID was used to concurrently record DF_{Cl} in GAD2+ interneurons in L1 of the anesthetized mouse brain (orange traces; bottom); inset: widefield fluorescence images of the cells from which the recordings of DF_{Cl} were made; scale bar: 10 µm. A variety of different DF_{Cl} values were recorded in different cells, including hyperpolarizing DF_{Cl} (left), shunting DF_{Cl} (center), and depolarizing DF_{Cl} (right). **c**, Population data showing DF_{Cl} in L1 interneurons in S1 (-0.3873 mV ± 0.5348 mV, n = 123 cells from 10 mice). **d**, 4-AP (500 µM) was infused into the cortex buffer in the recording chamber over the craniotomy (see **Methods**) to investigate DF_{Cl} dynamics during SLEs *in vivo*. Estimates of DF_{Cl} were made from GAD2+ interneurons before 4-AP wash-in (left; orange traces; wash-in labelled "4-AP"). 4-AP-induced SLEs were recorded in the LFP recording (black traces, purple bar indicates SLE), and recordings of DF_{Cl} were made again following the SLE (right). **e**, Population data of DF_{Cl} in GAD2+ interneurons showed a large depolarizing shift in DF_{Cl} post-SLE (paired t- test, $P < 0.0001$, n = 22 cells from 4 mice). ****$P \leq 0.0001$; error bars indicate mean ± SEM.

Discussion:

All-optical electrophysiology, combining voltage imaging and optogenetic stimulation, is a rapidly emerging strategy for studying neuronal dynamics in the intact nervous system[34,35]. Here we present the first all-optical strategy for studying ionic driving forces. We describe ORCHID, a powerful all-optical tool for the estimation of DF_{Cl}, the electromotive force for Cl^- flux across the membrane. Whilst ORCHID can conceivably be used to estimate DF_{Cl} in any cell type or organ, we validate its use in the nervous system. Taking advantage of ORCHID's ability to provide high-throughput, genetically targeted estimates of DF_{Cl} over extended periods of time, we confirm theoretical predictions regarding the mechanisms that establish DF_{Cl}, utilize ORCHID to reveal novel, cell-type-specific differences in activity-dependent DF_{Cl} changes during network activity, and provide the first *in vivo* measurements of intact DF_{Cl} in mouse cortical neurons.

ORCHID is easy to use with no spectral crosstalk between the orange excitation of the GEVI, $Voltron2_{608}$-ST, and blue-light activation of the integrated Cl^--permeable channel, GtACR2.

412 This means that ORCHID is compatible with a wide variety of experimental paradigms.
413 ORCHID's accuracy in reporting DF_{Cl} depends upon the amplitude of the light-activated Cl^-
414 conductance, relative to other conductances that are active in the cell of interest. For this
415 reason it is important that GtACR2 generates large transmembrane Cl^- conductances[23], and
416 any future optimization of light-activated Cl^- channels are predicted to further improve
417 ORCHID's accuracy. Whilst the permeability of GtACR2 to HCO_3^- has not been explicitly
418 measured, GtACR2's permeability sequence to other anions ($NO_3^- > I^- > Br^- > Cl^- > F^-$) is the
419 same as other Cl^- channels including $GABA_A$Rs and GlyRs[23–25], which exhibit a five-fold
420 greater permeability for Cl^- over HCO_3^-[24,25,36,37]. This is supported by the fact that reversal
421 potentials for GtACR2 and $GABA_A$Rs are equivalent[26,27], and also our evidence that ORCHID's
422 estimates of DF_{Cl} are comparable to those made by activating $GABA_A$Rs. In its current form
423 therefore, ORCHID provides an effective readout of the driving force across the Cl^- permeable
424 receptors that mediate fast synaptic inhibition in the brain. It is conceivable that future
425 developments could modulate the ion selectivity of light-activated Cl^- channels, which would
426 serve to enhance the accuracy of all-optical DF_{Cl} estimates.

427 ORCHID's all-optical approach has several powerful advantages over currently available
428 techniques for estimating DF_{Cl}. Firstly, and most fundamentally, ORCHID does not perturb
429 ionic gradients prior to measurement. Secondly, it is both genetically targetable and
430 addressable by light, which affords excellent temporal and spatial control. Thirdly, ORCHID's
431 high-throughput nature allows for measurements that are orders-of-magnitude faster than
432 traditional techniques. A typical gramicidin-perforated patch-clamp recording requires 30-60
433 minutes per cell, compared to 1-5 seconds per cell for an ORCHID recording. And fourthly,
434 ORCHID affords measurements from small cells and potentially subcellular compartments,
435 which are difficult, or impossible, to access using electrode-based techniques. In theory, a
436 fluorescent reporter of $[Cl^-]_i$ could also be used to report relative changes in DF_{Cl}, by measuring
437 changes in the amplitude of the $[Cl^-]_i$ response to an evoked Cl^- conductance[38]. However, this
438 is unlikely to be achieved in practice because of the inherent limitations in the sensitivity in Cl^-
439 imaging. Furthermore, detecting $[Cl^-]_i$ changes would require much larger and longer
440 conductances that alter $[Cl^-]_i$ in the cytoplasm, unlike ORCHID which only reflects Cl^-
441 movement across the membrane. By integrating a voltage-reporter element with the Cl^-
442 conductance, ORCHID's design makes it highly sensitive to transmembrane flux and offers
443 an intrinsic, simultaneous readout of the neuron's V_m.

444 Our results demonstrate how ORCHID strategies can be harnessed to test theoretical
445 predictions about the underlying mechanisms that establish ionic driving forces. Our
446 computational modelling and confirmatory empirical evidence support the accepted view that
447 DF_{Cl} is established by the action of CCCs such as KCC2[1]. Therefore, whilst genetically

448 encoded Cl^- indicators and other techniques that directly report $[Cl^-]_i$ are of considerable value,
449 ORCHID highlights the danger of interpreting $[Cl^-]_i$ changes in the context of inhibitory synaptic
450 transmission and DF_{Cl}, without a concurrent readout of V_m. This is particularly the case for
451 manipulations such as altering impermeant anions, which are predicted to shift both E_{Cl} and
452 V_m in tandem[31,39]. Given its ability to provide a sensitive readout of DF_{Cl}, we note that ORCHID
453 could serve as a high-throughput means for discovering new and improved enhancers, or
454 inhibitors, of transmembrane Cl^- transport.

455 Here we have utilized ORCHID to monitor unperturbed resting and dynamic DF_{Cl}. We confirm
456 and extend previous work by showing that intense network activity can induce a profound
457 change in DF_{Cl} polarity in neurons, with GABAergic synaptic input switching from inhibitory to
458 excitatory, which is relevant for the management of status epilepticus[40,41]. Whilst SLE-
459 associated DF_{Cl} estimates have been made using gramicidin-perforation in pyramidal
460 neurons[14], we provide the first data showing that inhibitory interneurons also undergo an
461 inversion in DF_{Cl} following seizure-like activity. Recent work has suggested that the transition
462 to seizures is associated with incremental increases in neuronal $[Cl^-]_i$, which is predicted to
463 reduce DF_{Cl} prior to seizure onset[32]. We provide direct evidence for this clinically relevant
464 phenomenon, and thereby demonstrate the utility of ORCHID in dynamically estimating DF_{Cl}
465 across network states.

466 By harnessing ORCHID's ability to be genetically targeted, we recorded resting DF_{Cl} from
467 several different cell types, including large populations of hippocampal CaMKIIα+ pyramidal
468 neurons, GAD2+ interneurons, and GFAP+ astrocytes. These results confirmed that
469 hippocampal neurons have hyperpolarizing resting DF_{Cl} *in vitro* and that this is the opposite to
470 astrocytes, which display a depolarizing resting DF_{Cl} that is in line with their differential
471 expression of CCCs[14,26,42]. It has been suggested that astrocytes could serve as a source of
472 extracellular Cl^- that helps to sustain the effectiveness of inhibitory GABAergic transmission[43],
473 which has recently been supported by direct measurements of astrocytic $[Cl^-]_i$ during periods
474 of network activity[44]. In support of this idea, our estimates of dynamic and intact DF_{Cl}
475 demonstrate that astrocytes are able maintain a force for the outward flux of Cl^-, even during
476 intense network activity. Cell-type-specific gene and protein expression data suggests that
477 other cell types including oligodendrocytes, ependymal cells, microglia, and endothelial cells,
478 all have specific expression patterns of CCCs[45]. ORCHID could therefore be used to
479 determine how these translate into differences in the available force for transmembrane Cl^-
480 fluxes in these and/or other cell types.

481 A further important question is how DF_{Cl} might be regulated at a subcellular level. For example,
482 it has been suggested that the properties of inhibitory synaptic input vary across a neuron and

483 between different cellular compartments[14,46–49]. However, this has been difficult to address
484 given the issue of space-clamp and other technical challenges associated with electrode-
485 based recordings. Future work could therefore combine ORCHID strategies with protein-
486 targeting motifs and the patterned delivery of light in order to record DF_{Cl} from difficult-to-
487 access subcellular compartments, such as distal apical dendrites, the axon initial segment,
488 and astrocytic processes. In a similar manner, one could imagine using targeted ORCHID
489 strategies to measure DF_{Cl} across the membranes of organelles, such as mitochondria,
490 lysosomes and vesicles. In doing so, ORCHID could be used to study a range of cellular
491 phenomena, including cell division, growth and migration, in which Cl^- fluxes across different
492 membranes contribute to the underlying intracellular and intercellular signaling processes.

493 Lastly, we have demonstrated how ORCHID has the ability to generate estimates of
494 undisturbed DF_{Cl} in the intact brain. Our *in vivo* results capture a range of DF_{Cl} values in cortical
495 L1 GAD2+ interneurons in S1 of the anesthetized mouse brain, which extends recent evidence
496 that $[Cl^-]_i$ and DF_{Cl} can vary as a function of sleep/wake history and brain state[10,11,50].
497 Furthermore, ORCHID reveals that DF_{Cl} is a dynamic parameter *in vivo*, with periods of intense
498 activity causing substantial shifts towards depolarizing DF_{Cl}. Whilst we have demonstrated
499 ORCHID's *in vivo* utility by imaging L1 interneurons, the approach could be extended to image
500 different cell populations throughout the mammalian brain[35]. Through the use of fiber
501 photometry, or the implementation of a GEVI that is suitable for use with 2-photon microscopy,
502 ORCHID has the potential to generate measurements of resting and dynamic DF_{Cl} in deep
503 brain structures, which has previously been impossible.

504 In conclusion, we establish ORCHID as an all-optical strategy for estimating DF_{Cl} in the
505 nervous system. This underscores the potential for similar all-optical strategies for elucidating
506 how ionic driving forces affect cellular signaling in a range of biological contexts.

References:

1. Kaila, K., Price, T. J., Payne, J. a., Puskarjov, M. & Voipio, J. Cation-chloride cotransporters in neuronal development, plasticity and disease. *Nat. Rev. Neurosci.* **15**, 637–654 (2014).
2. Kaila, K. Ionic basis of GABAA receptor channel function in the nervous system. *Prog. Neurobiol.* **42**, 489–537 (1994).
3. Wright, R., Raimondo, J. V. & Akerman, C. J. Spatial and temporal dynamics in the ionic driving force for GABA(A) receptors. *Neural Plast.* **2011**, 728395 (2011).
4. Raimondo, J. V., Richards, B. A. & Woodin, M. A. Neuronal chloride and excitability — the big impact of small changes. *Curr. Opin. Neurobiol.* **43**, 35–42 (2017).
5. Huberfeld, G. *et al.* Perturbed chloride homeostasis and GABAergic signaling in human temporal lobe epilepsy. *J Neurosci* **27**, 9866–73 (2007).
6. Hyde, T. M. *et al.* Expression of GABA signaling molecules KCC2, NKCC1, and GAD1 in cortical development and schizophrenia. *J Neurosci* **31**, 11088–95 (2011).
7. Price, T. J., Cervero, F., Gold, M. S., Hammond, D. L. & Prescott, S. A. Chloride regulation in the pain pathway. *Brain Res. Rev.* **60**, 149–170 (2009).
8. Tyzio, R. *et al.* Oxytocin-mediated GABA inhibition during delivery attenuates autism pathogenesis in rodent offspring. *Science* **343**, 675–9 (2014).
9. Ben-Ari, Y. Excitatory actions of GABA during development: the nature of the nurture. *Nat Rev Neurosci* **3**, 728–739 (2002).
10. Alfonsa, H. *et al.* Intracellular chloride regulation mediates local sleep pressure in the cortex. *Nat. Neurosci.* **26**, 64–78 (2023).
11. Pracucci, E. *et al.* Circadian rhythm in cortical chloride homeostasis underpins variation in network excitability. 2021.05.12.443725 Preprint at https://doi.org/10.1101/2021.05.12.443725 (2021).
12. Untiet, V. *et al.* Astrocytic chloride is brain state dependent and modulates inhibitory neurotransmission in mice. *Nat. Commun.* **14**, 1871 (2023).

13. Kyrozis, A. & Reichling, D. B. Perforated-patch recording with gramicidin avoids artifactual changes in intracellular chloride concentration. *J. Neurosci. Methods* **57**, 27–35 (1995).
14. Ellender, T. J., Raimondo, J. V., Irkle, A., Lamsa, K. P. & Akerman, C. J. Excitatory effects of parvalbumin-expressing interneurons maintain hippocampal epileptiform activity via synchronous afterdischarges. *J. Neurosci. Off. J. Soc. Neurosci.* **34**, 15208–22 (2014).
15. Verkman, A. S., Sellers, M. C., Chao, A. C., Leung, T. & Ketcham, R. Synthesis and characterization of improved chloride-sensitive fluorescent indicators for biological applications. *Anal. Biochem.* **178**, 355–361 (1989).
16. Weilinger, N. L. *et al.* KCC2 drives chloride microdomain formation in dendritic blebbing. *Cell Rep.* **41**, 111556 (2022).
17. Arosio, D. & Ratto, G. M. Twenty years of fluorescence imaging of intracellular chloride. *Front. Cell. Neurosci.* **8**, 1–12 (2014).
18. Arosio, D. *et al.* Simultaneous intracellular chloride and pH measurements using a GFP-based sensor. *Nat Methods* **7**, 516–8 (2010).
19. Kuner, T. & Augustine, G. J. A Genetically Encoded Ratiometric Indicator for Chloride: Capturing Chloride Transients in Cultured Hippocampal Neurons. *Neuron* **27**, 447–459 (2000).
20. Sulis Sato, S. *et al.* Simultaneous two-photon imaging of intracellular chloride concentration and pH in mouse pyramidal neurons in vivo. *Proc. Natl. Acad. Sci.* 201702861 (2017) doi:10.1073/pnas.1702861114.
21. Călin, A., Waseem, T., Raimondo, J. V., Newey, S. E. & Akerman, C. J. A genetically targeted ion sensor reveals distinct seizure-related chloride and pH dynamics in GABAergic interneuron populations. *iScience* **26**, 106363 (2023).
22. Abdelfattah, A. S. *et al.* Sensitivity optimization of a rhodopsin-based fluorescent voltage indicator. *Neuron* **111**, 1547-1563.e9 (2023).
23. Govorunova, E. G., Sineshchekov, O. A., Janz, R., Liu, X. & Spudich, J. L. Natural light-gated anion channels: A family of microbial rhodopsins for advanced optogenetics. *Science* **349**, 647–50 (2015).

24. Bormann, J., Hamill, O. P. & Sakmann, B. Mechanism of anion permeation through channels gated by glycine and gamma-aminobutyric acid in mouse cultured spinal neurones. *J. Physiol.* **385**, 243–286 (1987).
25. Fatima-Shad, K. & Barry, P. H. Anion permeation in GABA- and glycine-gated channels of mammalian cultured hippocampal neurons. *Proc. R. Soc. Lond. B Biol. Sci.* **253**, 69–75 (1993).
26. Burman, R. J. *et al.* Optogenetic determination of dynamic and cell-type-specific chloride equilibrium potentials. 2023.05.08.539831 Preprint at https://doi.org/10.1101/2023.05.08.539831 (2023).
27. Messier, J. E., Chen, H., Cai, Z.-L. & Xue, M. Targeting light-gated chloride channels to neuronal somatodendritic domain reduces their excitatory effect in the axon. *eLife* **7**, e38506 (2018).
28. Abdelfattah, A. S. *et al.* Bright and photostable chemigenetic indicators for extended in vivo voltage imaging. *Science* **365**, 699–704 (2019).
29. Grimm, J. B. *et al.* A general method to optimize and functionalize red-shifted rhodamine dyes. *Nat. Methods* **17**, 815–821 (2020).
30. Glykys, J., Dzhala, V., Egawa, K. & Balena, T. Local Impermeant Anions Establish the Neuronal Chloride Concentration. *Science* 670–676 (2014).
31. Düsterwald, K. M. *et al.* Biophysical models reveal the relative importance of transporter proteins and impermeant anions in chloride homeostasis. *eLife* **7**, 216150 (2018).
32. Graham, R. T. *et al.* Optogenetic stimulation reveals a latent tipping point in cortical networks during ictogenesis. *Brain* awac487 (2022) doi:10.1093/brain/awac487.
33. Rivera, C. *et al.* Mechanism of activity-dependent downregulation of the neuron-specific K-Cl cotransporter KCC2. *J Neurosci* **24**, 4683–91 (2004).
34. Hochbaum, D. R. *et al.* All-optical electrophysiology in mammalian neurons using engineered microbial rhodopsins. *Nat. Methods* **11**, 825–833 (2014).
35. Adam, Y. *et al.* Voltage imaging and optogenetics reveal behaviour-dependent changes in hippocampal dynamics. *Nature* **569**, 413–417 (2019).

36. Kaila, K., Pasternack, M., Saarikoski, J., Voipio, J. & Britain, G. Influence of GABA-gated bicarbonate conductance on potential, current and intracellular chloride in crayfish muscle fibres. *J Physiol* **416**, 161–181 (1989).
37. Kaila, K., Voipio, J., Paalasmaa, P., Pasternack, M. & Deisz, R. The role of bicarbonate in GABAA receptor-mediated IPSPs of rat neocortical neurones. *J. Physiol.* **464**, 273 (1993).
38. Grimley, J. S. *et al.* Visualization of synaptic inhibition with an optogenetic sensor developed by cell-free protein engineering automation. *J. Neurosci. Off. J. Soc. Neurosci.* **33**, 16297–309 (2013).
39. Voipio, J. *et al.* Comment on 'Local impermeant anions establish the neuronal chloride concentration'. *Science* **345**, 1130 (2014).
40. Burman, R. J. *et al.* Excitatory GABAergic signalling is associated with benzodiazepine resistance in status epilepticus. *Brain J. Neurol.* 478594 (2019) doi:10.1093/brain/awz283.
41. Burman, R. J. *et al.* Why won't it stop? The dynamics of benzodiazepine resistance in status epilepticus. *Nat. Rev. Neurol.* (2022) doi:10.1038/s41582-022-00664-3.
42. Ma, B.-F., Xie, M.-J. & Zhou, M. Bicarbonate efflux via GABA(A) receptors depolarizes membrane potential and inhibits two-pore domain potassium channels of astrocytes in rat hippocampal slices. *Glia* **60**, 1761–72 (2012).
43. Egawa, K., Yamada, J., Furukawa, T., Yanagawa, Y. & Fukuda, A. Cl^- homeodynamics in gap junction-coupled astrocytic networks on activation of GABAergic synapses. *J. Physiol.* **591**, 3901–3917 (2013).
44. Untiet, V. *et al.* Astrocytic chloride is brain state dependent and modulates inhibitory neurotransmission in mice. *Nat. Commun.* **14**, 1871 (2023).
45. Yao, Z. *et al.* A taxonomy of transcriptomic cell types across the isocortex and hippocampal formation. *Cell* **184**, 3222-3241.e26 (2021).
46. Duebel, J. *et al.* Two-photon imaging reveals somatodendritic chloride gradient in retinal ON-type bipolar cells expressing the biosensor Clomeleon. *Neuron* **49**, 81–94 (2006).
47. Szabadics, J. *et al.* Excitatory effect of GABAergic axo-axonic cells in cortical microcircuits. *Science* **311**, 233 (2006).

48. Glickfeld, L. L., Roberts, J. D., Somogyi, P. & Scanziani, M. Interneurons hyperpolarize pyramidal cells along their entire somatodendritic axis. *Nat. Neurosci.* **12**, 21–3 (2009).
49. Földy, C., Lee, S.-H., Morgan, R. J. & Soltesz, I. Regulation of fast-spiking basket cell synapses by the chloride channel ClC-2. *Nat Neurosci* **13**, 1047–9 (2010).
50. Burman, R. J., Brodersen, P. J. N., Raimondo, J. V., Sen, A. & Akerman, C. J. *Active cortical networks promote shunting fast synaptic inhibition* in vivo. http://biorxiv.org/lookup/doi/10.1101/2023.03.01.530641 (2023) doi:10.1101/2023.03.01.530641.

Methods:

ORCHID construct subcloning

The ORCHID construct combined GtACR2 from the pAAV-EF1α-FRT-FLEX-GtACR2-EYFP plasmid, which was a gift from Mingshan Xue (Addgene plasmid #114369) (Messier *et al.*, 2018), with Voltron2-ST from the pGP-pcDNA3.1 Puro-CAG-Voltron2-ST plasmid (Abdelfattah *et al.*, 2023), which was kindly provided by Eric Schreiter and Ahmed Abdelfattah. The two genes were linked by a P2A linker sequence identical to that used by Holst *et al.* (2006) to form an insert sequence, and include the Kozak sequence 5' GCCACC(ATG) 3'. The vector used for the ORCHID construct originated from pAAV-hSyn-DIO {ChETA-mRuby2}on-W3SL, which was a gift from Adam Kepecs (Addgene plasmid #111389) (Li *et al.*, 2018), with the hSyn promoter replaced with the EF-1α promoter from pAAV-nEF Con/Foff hChR2(H134R)-EYFP, which was a gift from Karl Deisseroth (Addgene plasmid #55647) (Fenno *et al.*, 2014). The GtACR2-P2A-Voltron2-ST sequence of the ORCHID construct was synthesized in antisense (Thermo Fisher Scientific GeneArt Gene Synthesis) and inserted into the vector using the Bsp1407I/NheI restriction enzyme sites and the FastDigest versions of the two enzymes (Thermo Fisher Scientific). Sanger sequencing confirmed the sequence of the final construct. Production of the AAV vector (serotype 1) containing the completed pAAV-nEF-DIO-GtACR2-P2A-Voltron2ST-W3SL construct was carried out by Dr R. Jude Samulski and the University of North Carolina Vector Core.

Mouse hippocampal organotypic brain slice cultures

The animals used in this study were wild-type (C57BL/6 background) or GAD2-IRES-Cre mice (RRID:IMSR_JAX:010802), with the GAD2-IRES-Cre strain being characterized by expression of Cre recombinase in all GABAergic interneurons. The use of these animals was approved by the University of Cape Town Animal Ethics Committee (AEC Protocol 021/026 and AEC Protocol 022/038). Organotypic brain slice cultures were prepared using postnatal day (P) 7 mice and followed the protocol originally described by Stoppini, Buchs and Muller (1991) [for details see Raimondo *et al.* (2016)] All reagents were purchased from Sigma-Aldrich unless otherwise stated. Briefly, the mice were killed, and the brains were removed and placed in 4°C Earle's Balanced Salt Solution (EBSS), with 6.1 g/l HEPES, 6.6 g/l glucose, and 5% 1 M NaOH. The hippocampi were removed and sectioned into 350 µm slices using a tissue chopper (McIlwain). The slices were placed on Millicell-CM membranes and cultured in medium consisting of (v/v): 25% EBSS; 49% minimum essential medium; 25% heat-inactivated horse serum; 1% B27 (Invitrogen, Life Technologies), and 6.2 g/l D-glucose. The slices were incubated at 35-37°C in a 5% CO_2 humidified incubator.

Viral transfection was performed at 0-1 days *in vitro* (DIV). For experiments in which endogenous $GABA_A$Rs were activated, pGP-AAV-syn-flex-Voltron2-ST-WPRE-SV40 was utilized, while for ORCHID experiments pAAV-nEF-DIO-GtACR2-P2A-Voltron2ST-W3SL was utilized. AAV-CaMKIIα-Cre-GFP and AAV8-GFAP-GFP-Cre were used to target CaMKIIα+ pyramidal neurons and GFAP+ astrocytes respectively. Here, as in all relevant methods, micropipettes were prepared from borosilicate glass capillaries (Warner Instruments). The AAVs were loaded into a glass micropipette along with FastGreen (0.1% w/v) to aid visualization, and were injected into the slices using the Openspritzer system (Forman *et al.*, 2017). Biolistic transfection was performed at 4-5 DIV. Cartridges were prepared as described by O'Brien and Lummis (2006), using 20 mg of pGP-pcDNA3.1 Puro-CAG-Voltron2-ST plasmid DNA and 1.6 µm gold microcarriers (Bio-Rad). Slices were transfected using a 3D-printed version of the modified barrel design (O'brien *et al.*, 2001).

Recordings were performed at 7-14 DIV, which is equivalent to P14-21. This, as well as previous work, has shown that pyramidal neurons in the organotypic slices of the hippocampus have mature and stable Cl^- homeostasis mechanisms at this stage, as evidenced by their hyperpolarizing DF_{Cl} (Streit, Thompson and Gähwiler, 1989; Ilie, Raimondo and Akerman, 2012; Raimondo *et al.*, 2012; Wright *et al.*, 2017). Prior to imaging, slices were incubated for 30 min in aCSF bubbled with carbogen gas (95% O_2: 5% CO_2), containing either JF_{549} or JFX_{608} dye at 1 mM. The aCSF was composed of (in mM): NaCl (120); KCl (3); $MgCl_2$ (2); $CaCl_2$ (2); NaH_2PO_4 (1.2); $NaHCO_3$ (23); and D-glucose (11). During this incubation step the dye binds irreversibly to the Voltron2-ST protein (Abdelfattah *et al.*, 2019). After the incubation was complete, slices were transferred to a submerged recording chamber where they were continuously superfused with 32°C carbogen-bubbled aCSF using a peristaltic pump (Watson-Marlow). Pharmacological agents included CGP-55845 (5 µM) and 2-chloroadenosine (4 µM) in the recording aCSF for all experiments in which $GABA_A$Rs were activated, as well as pictrotoxin (PTX; 100 µM), VU0463271 (VU; 10 µM), 4-aminopyradine (4-AP, 50 µM), and tetrodotoxin (TTX; 1 µM) for subsets of the *in vitro* experiments.

Surgical procedures for in vivo imaging

Intracranial bulk regional viral injections of pAAV-nEF-DIO-GtACR2-P2A-Voltron2-ST-W3SL were performed on P0-1 GAD2-IRES-Cre mouse pups (Cheetham, Grier and Belluscio, 2015; Oomoto *et al.*, 2021). Adult breeders were removed from the home cage and placed in a holding cage for the duration of the procedure. A 30G insulin syringe was loaded with 1 µl AAV combined with FastGreen (0.1% w/v) to aid visualization and mounted in a stereotaxic frame. Pups were individually removed from their home cage and anesthetized using 2 ml isoflurane pipetted onto a gauze swab in an enclosed space. Respiration rate and skin color

were monitored to assess depth of anesthesia. Once depth of anesthesia was sufficient, pups were rapidly transferred to a heating pad beneath the stereotaxic frame and the AAV was injected into S1 of the left cerebral hemisphere at a depth of 1-2 mm, with a successful injection indicated by green coloration of the hemisphere. The injection typically took ~30 s. The pup was then transferred back to its home cage and monitored until fully recovered from anesthesia, when the injection of the next pup was begun. We observed a 100% survival rate of injected pups using this method.

Imaging experiments began after P28. Retroorbital injections of JF_{608} were performed 3-24 h prior to imaging (Abdelfattah *et al.*, 2019, 2023). 100 nmol JF_{608} was dissolved in 20 µl DMSO, 20 µl Pluronic F-127 (20% w/v in DMSO, Thermo Fisher Scientific), and 60 µl sterile phosphate-buffered saline (PBS). The mice were anesthetized using an intraperitoneal (IP) injection of ketamine/xylazine mixture (ketamine 80 mg/kg and xylazine 10 mg/kg). The JF_{608} solution was delivered using a 30G insulin syringe as described by Yardeni *et al.* (2011). The preparation for anesthetized recordings was adapted from Burman *et al.* (2023). Mice were anesthetized using 3 l/s O_2 with 5% isoflurane for induction, and with the isoflurane reduced to 1-2% for maintenance. Once anesthetized, the animal was secured in a stereotaxic frame (Narishige). An IP injection of buprenorphine (0.5 mg/kg) and a subcutaneous (SC) injection of 200 µl sterile saline were administered for analgesia and hydration respectively. The mouse's body temperature was maintained at ~37°C using a heating pad and a temperature probe. The head was shaved, and eye-protecting ointment (Duratears) was applied to each eye. An incision in the scalp was made using surgical scissors and the area was expanded by blunt dissection to expose the skull. Forceps were used to remove any membranous tissue from the surface of the skull. Tissue adhesive (Vetbond) was used to fix the edges of the incised scalp to the skull and to stabilize the cranial sutures. Several layers of dental cement (InterDent) were applied to create a recording chamber on top of the skull. A 0.5 mm craniotomy was drilled over S1 using a dental drill (Dental Lab). The craniotomy was submerged in cortex buffer containing (in mM): NaCl (125), KCl (5), HEPES (10), $MgSO_4 \cdot 7H_2O$ (2), $CaCl_2 \cdot 2H_2O$ (2), D-glucose (10). The bone flap and dura were removed. The mouse was then transferred to the imaging setup. In a subset of animals, 4-AP was infused into the cortex buffer in the recording chamber using a pipette (500 µM working concentration). The recording session typically lasted 3 h.

Electrophysiology

For patch-clamp recordings, micropipettes were filled with a low-Cl^- internal solution composed of (in mM): K-gluconate (120); KCl (10); Na_2ATP (4); NaGTP (0.3); Na_2-phosphocreatinine (10) and HEPES (10). For high-Cl^- recordings, pipettes were filled with a high-Cl^- internal

solution ([Cl^-] = 141 mM) composed of (in mM): KCl (135), NaCl (8.9) and HEPES (10). Recordings were made using an Axopatch 200B amplifier (Molecular Devices) and data was acquired using WinWCP (University of Strathclyde). For experiments investigating the role of impermeant anions in setting DF_{Cl}, anionic 10 000 MW dextran bound to Alexa-Flour 488 (Thermo Fisher Scientific) was electroporated into cells. This molecule is a hydrophilic polysaccharide, being both membrane impermeant and having a large negative average charge. A micropipette was filled with 5% dextran solution in PBS, and the micropipette was positioned near the soma of the targeted neuron. Voltage pulses (5-10 pulses, 20 ms duration, 0.5-1 V) were applied using a stimulus isolator, and successful electroporation was confirmed visually by observing the neuron filled with the fluorescent dye. For *in vivo* LFP recordings, micropipettes were filled with cortex buffer. The tip of the pipette was broken against tissue paper with the aim of achieving a tip diameter of ~5 µm. Recordings were made using a differential amplifier (A-M system, 1800) and data was acquired using LabChart (ADInstruments).

Widefield fluorescence imaging

Neurons were visualized using a BX51WI upright microscope (Olympus) equipped with a 20x water-immersion objective (Olympus XLUMPlanFL) and a sCMOS camera (Andor Zyla 4.2). For imaging Voltron2$_{549}$-ST, a green LED with a 555/28 nm excitation filter (Lumencor Aura III) was used for excitation (20.6 mW/mm^2) with a further multi-band filter set for collecting emission between 590 and 660 nm (Chroma, 69401-ET-380/55-470/30-557/35 multi LED). For Voltron2$_{608}$-ST or ORCHID, a high-powered orange LED (590 nm, SOLIS-590C, Thorlabs) was used for excitation (143 mW/mm^2). Optogenetic activation of GtACR2 as a part of ORCHID was achieved using a blue LED (475/28 nm, Lumencor Aura III), with the intensity of this LED fixed at 3.6 mW/mm^2. A T570lpxr beam splitter was used for combining the blue and orange LEDs, before a filter set with a 599/13 nm excitation filter, a 612 nm long pass beam splitter, and a 632/28 nm emission filter was used (Chroma, 49311-ET-Red#3 Narrow band FISH).

Illumination of the tissue was restricted to a 140 µm diameter region using the built-in Olympus variable-diameter field stop aperture. Image acquisition was controlled using µManager. For current-step recordings, exposure was 5 ms with an image acquisition frequency of 200 Hz. For all voltage-step recordings and Voltron2$_{549}$-ST recordings, exposure was 10 ms and image acquisition frequency was 100 Hz. For ORCHID recordings exposure was 20 ms and image acquisition frequency was 25 Hz. The imaging region was 256 x 256 pixels, and with no overlap between successive camera exposures this ensured a 20 ms gap between successive exposures. Transistor-transistor logic (TTL) signals from the camera were set to output

throughout the exposure, and this signal was sent to an Arduino that ran a custom script to activate the blue LED immediately after each camera exposure ended and for 15 ms, allowing for a 5 ms gap between the blue LED being switched off and the subsequent camera exposure. We found this to be crucial for artefact-free imaging. Camera acquisition and blue-light activation were thus both at a frequency of 25 Hz, with 50% and 37.5% on-time respectively.

When utilizing Voltron2$_{549}$-ST with GABA$_A$R activation, 500 µM GABA in recording aCSF was loaded into a micropipette and 100 ms puffs of synthetic air were delivered to the micropipette using the Openspritzer system. Imaging traces were 7 s long with a 1 s baseline period prior to the puff. Care was taken to ensure no movement artefact from the puff. ORCHID recordings had a duration of 25 s and consisted of five 1 s or 2 s strobed optogenetic activations, which were averaged post-hoc for some experiments (see Data Analysis and Statistics). During low-Mg^{2+} wash-ins, in order to increase the chance of recording a SLE, the duration of recordings was increased to 65 s, and ORCHID was activated with 1 s periods of strobed light every 5 s. SLEs were defined as events with significant deviation from the resting potential in patch-clamp recordings (> 2 standard deviations) lasting for at least 5 s.

Confocal imaging

Confocal images of live brain slices were obtained on a LSM 880 Airyscan confocal microscope (Carl Zeiss, ZEN SP 2 software) using a C-Apochromat 40x objective.

Single-nucleus RNA sequencing

Nuclei from mouse hippocampal organotypic hippocampal brain slices were dissociated in lysis buffer (Nuclei EZ Prep, NUC101) on ice and processed via the 10X Genomics platform to prepare libraries for sequencing as outlined in the Chromium Next GEM 3' Single Cell 3 Reagent Kits v3.1 user guide. Four samples, each comprising 36 hippocampal slices, were processed. Libraries were sequenced using a Illumina NovaSeq 6000 S2 flow cell. Analysis of the snRNAseq data was performed on facilities provided by the University of Cape Town's ICTS High Performance Computing team. Cell Ranger version 7.1.0 was used to map paired-end sequencing reads to the mouse reference transcriptome (refdata-gex-mm10-2020-A). The filtered feature-barcode matrix of each sample was converted into a Seurat object. Samples were processed according to the standard Seurat pipeline in R (Hao *et al.*, 2021).

Quality control (QC) involved removing nuclei with less than 500 unique molecular identifiers (UMIs), fewer than 250 genes expressed, log10GenesPerUMI less than 0.8, and/or a mitochondrial ratio greater than 0.2. Additionally, all mitochondrial genes were excluded from the dataset. Three doublet identification tools were employed, including DoubletFinder (McGinnis, Murrow and Gartner, 2019), Scrublet (Wolock, Lopez and Klein, 2019), and

DoubletDecon (DePasquale *et al.*, 2019). For each sample, all doublets called by DoubletFinder together with the intersection of doublets called by Scrublet and DoubletDecon were filtered out. Following QC, normalization and variance stabilization were performed using the SCTransform() function. The mitochondrial ratio was regressed out during this step. Integration of the different samples was performed via Seurat's FindIntegrationAnchors() function using the top 2000 most variable features and 30 dimensions followed by the IntegrateData() function. A principle component analysis (PCA) was run on the integrated data followed by clustering using the FindNeighbors() and FindClusters() functions.

Several cluster annotation approaches were employed including automated annotation, manual annotation, and Seurat's label transfer method. For automated annotation, Seurat's FindAllMarkers() function was used to identify differentially expressed genes (DEGs) between the clusters. A cluster resolution of 0.4 was set as the active identity and comprised 30 clusters to be annotated. An automated annotation tool known as SCSA (Cao, Wang and Peng, 2020) was used to obtain putative cluster annotations by comparing the list of DEGs per cluster obtained from FindAllMarkers() to reference datasets of known cell-type-specific markers including SCSA's built-in reference databases (Zhang *et al.*, 2019) as well as user-defined databases curated from mousebrain.org (Zeisel *et al.*, 2018). Manual inspection methods involved visualizing the expression of a smaller set of known cell-type-specific markers across the different clusters in bubbleplots as well as searching for the cell-type-specific markers in the list of cluster-specific DEGs from the FindAllMarkers() output. Using the automated and manual annotation method, putative user-defined annotations for each cluster were generated. Additionally, Seurat's label transfer method was carried out using the Allen Mouse Brain atlas as the reference (Yao *et al.*, 2021). Seurat's FindTransferAnchors() function was used to find anchors between the reference and query datasets with "SCT" specified as the normalization method and the top 30 dimensions used. A relatively stringent filtering step was then performed to remove any nuclei that did not have agreement between their broad user-defined and Allen Mouse Brain annotations. Following this filtering step, the user-defined coarse annotations were used for downstream analyses. The 4 control samples were subsetted and heatmaps were plotted to visualize the normalized average expression of several genes of interest across the pyramidal neuron and astrocyte clusters respectively.

Data analysis and statistics

Data analysis was performed using custom scripts written in MATLAB (MathWorks). The image analysis pipeline extracted signals from a region of interest (ROI) targeted to the soma of the cell and calculated an integrated density of fluorescence (i.e., mean pixel brightness) in this region (F_s). Background subtraction was performed by selecting a ROI targeted to a

representative area of the background, calculating an integrated density of fluorescence in this region, and subtracting this from F_s image-wise. For ORCHID recordings this background fluorescence signal was smoothed with a smoothing window of 100 before being subtracted from F_s. Correction for photobleaching and low-frequency changes in signal was performed by fitting and subtracting a 9th- or 10th-order polynomial to and from the background-corrected F_s trace. The response to the GABA puff or optogenetic stimulation in the F_s trace was excluded from the fitting of this polynomial to avoid removing the signal from the trace. For recordings using Voltron2$_{549}$-ST with $GABA_AR$ activation this corrected F_s trace was smoothed with a smoothing window of 7, and $\Delta F/F_0$ values were calculated using the maximum or minimum value of the smoothed signal post-puff and the mean of the smoothed baseline period prior to the puff. This same process was used for ORCHID recordings during activity-dependent variation in DF_{Cl} experiments, with the maximum or minimum value of the smoothed signal during an optogenetic stimulation being used to calculate $\Delta F/F_0$. For all other *in vitro* ORCHID recordings, the 5 strobed optogenetic stimulation periods in the F_s trace were averaged before $\Delta F/F_0$ was calculated using the mean during averaged optogenetic stimulation and the mean during the averaged baseline period prior to optogenetic stimulation onset. Due to the higher levels of spontaneous activity *in vivo*, for *in vivo* ORCHID recordings ΔF and F_0 were calculated using the mean fluorescence during a single optogenetic stimulus and an equivalent duration of recording on one side of the stimulus (these values termed ΔF_S and F_{0S}). To correct for neuropil contamination, the indices of these two periods (the period during the stimulus and the baseline period) were used to calculate an equivalent ΔF from the background fluorescence trace (ΔF_{BG}), which was subtracted from ΔF_S (giving $\Delta F_{S\text{-}BG}$). $\Delta F/F_0$ was then calculated using $\Delta F_{S\text{-}BG}$ and F_{0S}. Using the linear fluorescence changes recorded in response to voltage steps (**Fig. 1i,j** and **Supplementary Figure 3c,d**), estimated DF_{Cl} was calculated from $\Delta F/F_0$. Statistical measurements were performed using GraphPad Prism. The Shapiro-Wilk test was used to test for normality, and parametric or non-parametric tests were selected as required. Data is reported as mean ± SEM unless stated otherwise.

Computational Model

We simulated a neuron using the pump-leak mechanism as a single compartment within an extracellular environment consisting of fixed ion concentrations ("infinite bath model"). The compartment was modelled as a cylinder with a diameter of 1 µm and a length of 25 µm. Ionic flow between the compartment and external environment was permitted via leak channels, a Na^+/K^+-ATPase, and KCC2 transporters. For details of the simulation equations for ionic flux and volume change, see Düsterwald *et al.* (2018). In addition, $GABA_ARs$, HCO_3^- and pH regulation were added to the model in Düsterwald *et al.* (2018), which we describe below.

Fast GABAergic synaptic transmission mediated by $GABA_A$Rs was modelled using the kinetic binding model described by Destexhe *et al.* (1993), where the ratio of bound to unbound receptors (*r*) is a function of the rate of neurotransmitter binding (α), unbinding (β), and maximal neurotransmitter concentration ([$GABA_{Max}$]):

$$\frac{dr}{dt} = \alpha\,[GABA_{Max}](1-r) - \beta r$$

Current through $GABA_A$Rs (I_{GABAA}) was modelled as follows:

$$I_{GABAA} = I_{GABA_{Cl^-}} + I_{GABA_{HCO_3^-}}$$

$$I_{GABA_{Cl^-}} = \chi \cdot g_{GABAA} \cdot r_t \cdot (V_m - E_{Cl^-})$$

$$I_{GABA_HCO_3^-} = (1-\chi) \cdot\ g_{GABAA} \cdot r_t \cdot \left(V_m - E_{HCO_3^-}\right)$$

The bound receptor ratio at a particular time point (r_t) was used to calculate the instantaneous current through the $GABA_A$R channel, where g_{GABAA} refers to the conductance of the channel. χ represents the fraction of the total GABAergic current carried by Cl^- and is given by:

$$\chi = \frac{E_{HCO_3^-} - E_{GABAA}}{E_{HCO_3^-} - E_{Cl^-}}$$

where the reversal potential for Cl^- (E_{Cl^-}), HCO_3^- and the $GABA_A$ receptor (E_{GABAA}) were updated, where applicable, throughout the simulation using the Nernst and Goldman-Hodgkin-Katz equations, respectively:

$$E_{Cl^-} = \frac{R \cdot T}{F} ln\left(\frac{[Cl^-]_i}{[Cl^-]_o}\right)$$

$$E_{HCO_3^-} = \frac{R \cdot T}{F} \ln\left(\frac{[HCO_3^-]_i}{[HCO_3^-]_o}\right)$$

$$E_{GABAA} = \frac{R \cdot T}{F} ln\left(\frac{\frac{4}{5}[Cl^-]_i + \frac{1}{5}[HCO_3^-]_i}{\frac{4}{5}[Cl^-]_o + \frac{1}{5}[HCO_3^-]_o}\right)$$

where R is the ideal gas constant, F is Faraday's constant, and T is temperature.

Carbon dioxide was assumed to be equilibrium distributed across the simulated plasma membrane and the CO_2 hydration reaction inside and outside the compartment was also assumed to be under equilibrium.

$$H_2O + CO_2 \rightleftharpoons\ H_2CO_3 \rightleftharpoons\ H^+ + HCO_3^-$$

For a pCO_2 of 38 mmHg (5% CO_2), $[CO_2]$ was calculated using Henry's Law and a Henry's Law constant for CO_2 in water of 0.031 (M/atm).

$$[CO_2] = kH \cdot pCO_2$$

Assuming that $[CO_2] \approx [H_2CO_3]$, using the Henderson Hasselbalch equation and a pK_a of 6.1 as the dissociation constant for H_2CO_3, $[HCO_3^-]$ was calculated at pH of 7.4 (outside) and at a pH of 7.1 (inside) using:

$$[HCO_3^-] = [H_2CO_3] \times 10^{pH-pK_a}$$

giving a $[HCO_3^-]_o$ = 31 mM and a $[HCO_3^-]_i$ = 15.0 mM.

In the simulation pH was held constant. Transmembrane flux of HCO_3^- via $GABA_A$Rs (I_{GABA_HCO3-}), was assumed to be immediately regenerated by the forward CO_2 hydration reaction producing a matching additional number of H^+, which, to maintain pH, was simulated as being immediately exchanged with Na^+ via the Na^+/H^+ exchanger (Chesler, 2003).

Parameters:

Symbol	Value	Description
Constants		
F	96485.33 C/mol	Faraday constant
R	8.31446 J/(K·mol)	Universal gas constant
T	310.15 K	Absolute temperature (= 37°C)
Parameters		
Radius	5 µm	Radius of the single compartment
Length	25 µm	Length of the single compartment
C_m	2 x10^{-6} F/cm^2	Unit membrane capacitance (Qian and Sejnowski, 1989)
g_{Na}	31.1 µS/cm^2	Na^+ leak conductance
g_K	70 µS/cm^2	K^+ leak conductance
g_{Cl}	20 µS/cm^2	Cl^- leak conductance
g_{KCC2}	120 µS/cm^2	KCC2 conductance

v_w	0.018 dm^3/mol	Partial molar volume of water (Hernández and Cristina, 1998)
p_w	0.0015 dm/s	Osmotic permeability (Hernández and Cristina, 1998)
P	0.1 $C/(dm^2 \cdot s)$	ATPase pump rate constant
α	0.5 $ms^{-1}mM^{-1}$	Forward rate constant for GABA binding (Destexhe, Mainen and Sejnowski, 1993).
β	0.1 ms^{-1}	Reverse rate constant for GABA binding (Destexhe, Mainen and Sejnowski, 1993).
$GABA_{Max}$	30 mM	Saturating concentration of GABA.
g_{GABAA}	10 nS	Maximum conductance of $GABA_A$Rs.
pH_o	7.4	Extracellular pH
pH_i	7.1	Intracellular pH
$[Na^+]_o$	145 mM	Extracellular Na^+ conc.
$[Na^+]_i$	14 mM	Initial intracellular Na^+ conc.
$[K^+]_o$	3.5 mM	Extracellular K^+ conc.
$[K^+]_i$	122.9 mM	Initial intracellular K^+ conc.
$[HCO_3^-]_o$	31 mM	Extracellular HCO_3^- conc.
$[HCO_3^-]_i$	15 mM	Intracellular HCO_3^- conc.
$[Cl^-]_o$	108 mM	Extracellular Cl^- conc.
$[Cl^-]_i$	5.2 mM	Initial intracellular Cl^- conc.
$[X^-]_o$	40.5 mM	Extracellular impermeant anion conc.
$[X^-]_i$	154.9 mM	Initial intracellular impermeant anion conc.
z_o	-1	Extracellular impermeant anion average charge
z_i	-0.85	Initial intracellular impermeant anion average charge (Lodish et al. 2009)

Code used for the simulations is accessible at: https://github.com/Eran707/ORCHID-code-repository.

References for Methods:

Abdelfattah, A.S. *et al.* (2019) 'Bright and photostable chemigenetic indicators for extended in vivo voltage imaging', *Science*, 365(6454), pp. 699–704.

Abdelfattah, A.S. *et al.* (2023) 'Sensitivity optimization of a rhodopsin-based fluorescent voltage indicator', *Neuron*, 111(10), pp. 1547-1563.e9.

Burman, R.J. *et al.* (2023) *Active cortical networks promote shunting fast synaptic inhibition* in vivo. preprint. Neuroscience.

Cao, Y., Wang, X. and Peng, G. (2020) 'SCSA: A Cell Type Annotation Tool for Single-Cell RNA-seq Data', *Frontiers in Genetics*, 11.

Cheetham, C.E.J., Grier, B.D. and Belluscio, L. (2015) 'Bulk regional viral injection in neonatal mice enables structural and functional interrogation of defined neuronal populations throughout targeted brain areas', *Frontiers in Neural Circuits*, 9(November), pp. 1–13.

Chesler, M. (2003) 'Regulation and modulation of pH in the brain', *Physiol. Rev.*, 83(4), pp. 1183–221.

Dai, J. *et al.* (1998) 'Membrane Tension in Swelling and Shrinking Molluscan Neurons', *The Journal of Neuroscience*, 18(17), pp. 6681–6692.

DePasquale, E.A.K. *et al.* (2019) 'DoubletDecon: Deconvoluting Doublets from Single-Cell RNA-Sequencing Data', *Cell Reports*, 29(6), pp. 1718-1727.e8.

Destexhe, A., Mainen, Z.F. and Sejnowski, T.J. (1993) 'An Efficient Method for Computing Synaptic Conductances Based on a Kinetic Model of Receptor Binding', p. 4.

Doyon, N. *et al.* (2016) 'Chloride Regulation: A Dynamic Equilibrium Crucial for Synaptic Inhibition', *Neuron*, 89(6), pp. 1157–1172.

Düsterwald, K.M. *et al.* (2018) 'Biophysical models reveal the relative importance of transporter proteins and impermeant anions in chloride homeostasis', *eLife*, 7, p. e39575.

Fenno, L.E. *et al.* (2014) 'Targeting cells with single vectors using multiple-feature Boolean logic', *Nature Methods*, 11(7), pp. 763–772.

Forman, C.J. *et al.* (2017) 'Openspritzer: An open hardware pressure ejection system for reliably delivering picolitre volumes', *Scientific Reports*, 7(1), pp. 1–11.

Hao, Y. *et al.* (2021) 'Integrated analysis of multimodal single-cell data', *Cell*, 184(13), pp. 3573-3587.e29.

Hernández, J.A. and Cristina, E. (1998) 'Modeling cell volume regulation in nonexcitable cells: the roles of the Na+ pump and of cotransport systems', *American Journal of Physiology - Cell Physiology*, 275(4), pp. C1067–C1080.

Hille, B. (2001) 'Ion Channels of Excitable Membranes', *Sunderland Massachusetts USA*.

Holst, J. *et al.* (2006) 'Rapid analysis of T-cell selection in vivo using T cell–receptor retrogenic mice', *Nature Methods*, 3(3), pp. 191–197.

Ilie, A., Raimondo, J.V. and Akerman, C.J. (2012) 'Adenosine Release during Seizures Attenuates GABAA Receptor-Mediated Depolarization', *Journal of Neuroscience*, 32(15), pp. 5321–5332.

Li, S.-J. *et al.* (2018) 'A Viral Receptor Complementation Strategy to Overcome CAV-2 Tropism for Efficient Retrograde Targeting of Neurons', *Neuron*, 98(5), pp. 905-917.e5.

Lodish, H. *et al.* (2009) 'Intracellular Ion Environment and Membrane Electric Potential', in *Molecular Cell Biology*. 4th edn. New York.

McGinnis, C.S., Murrow, L.M. and Gartner, Z.J. (2019) 'DoubletFinder: Doublet Detection in Single-Cell RNA Sequencing Data Using Artificial Nearest Neighbors', *Cell Systems*, 8(4), pp. 329-337.e4.

Messier, J.E. *et al.* (2018) 'Targeting light-gated chloride channels to neuronal somatodendritic domain reduces their excitatory effect in the axon', *eLife*. Edited by I.M. Raman and G.L. Westbrook, 7, p. e38506.

O'brien, J.A. *et al.* (2001) 'Modifications to the hand-held Gene Gun: Improvements for in vitro biolistic transfection of organotypic neuronal tissue', *Journal of Neuroscience Methods*, 112(1), pp. 57–64.

O'Brien, J.A. and Lummis, S.C.R. (2006) 'Biolistic transfection of neuronal cultures using a hand-held gene gun', *Nature Protocols*, 1(2), pp. 977–981.

Oomoto, I. *et al.* (2021) 'Protocol for cortical-wide field-of-view two-photon imaging with quick neonatal adeno-associated virus injection', *STAR Protocols*, 2(4), p. 101007.

Qian, N. and Sejnowski, T.J. (1989) 'An Electro-Diffusion Model for Computing Membrane Potentials and Ionic Concentrations in Branching Dendrites, Spines and Axons', *Biological Cybernetics*, 62(1), pp. 1–15.

Raimondo, J.V. *et al.* (2012) 'Optogenetic silencing strategies differ in their effects on inhibitory synaptic transmission', *Nature Neuroscience*, 15(8), pp. 1102–1104.

Raimondo, J. V. *et al.* (2015) 'Ion dynamics during seizures', *Frontiers in Cellular Neuroscience*, 9(October), pp. 1–14.

Raimondo, J.V. *et al.* (2016) 'Tight Coupling of Astrocyte pH Dynamics to Epileptiform Activity Revealed by Genetically Encoded pH Sensors', *Journal of Neuroscience*, 36(26), pp. 7002–7013.

Stoppini, L., Buchs, P.A. and Muller, D. (1991) 'A simple method for organotypic cultures of nervous tissue', *Journal of Neuroscience Methods*, 37(2), pp. 173–182.

Streit, P., Thompson, S.M. and Gähwiler, B.H. (1989) 'Anatomical and Physiological Properties of GABAergic Neurotransmission in Organotypic Slice Cultures of Rat Hippocampus', *European Journal of Neuroscience*, 1(6), pp. 603–615.

Wolock, S.L., Lopez, R. and Klein, A.M. (2019) 'Scrublet: Computational Identification of Cell Doublets in Single-Cell Transcriptomic Data', *Cell Systems*, 8(4), pp. 281-291.e9.

Wright, R. *et al.* (2017) 'Neuronal Chloride Regulation via KCC2 Is Modulated through a GABAB Receptor Protein Complex'.

Yao, Z. *et al.* (2021) 'A taxonomy of transcriptomic cell types across the isocortex and hippocampal formation', *Cell*, 184(12), pp. 3222-3241.e26.

Yardeni, T. *et al.* (2011) 'Retro-orbital injections in mice', *Lab Animal*, 40(5), pp. 155–160.

Zeisel, A. *et al.* (2018) 'Molecular Architecture of the Mouse Nervous System', *Cell*, 174(4), pp. 999-1014.e22.

Zhang, X. *et al.* (2019) 'CellMarker: a manually curated resource of cell markers in human and mouse', *Nucleic Acids Research*, 47(D1), pp. D721–D728.

Data and code availability:

All data was analyzed using custom scripts created in Matlab. Code will be made publically available on GitHub upon publication, but until then is available upon request. Source data will be published alongside the publication of the manuscript and raw data is available upon reasonable request.

Acknowledgements:

We would like to thank members of the Raimondo lab for advice and comments and to Suzanne Duncan with assistance naming ORCHID.
We thank Sarah E. Plutkis, Katie L. Holland, Jonathan B. Grimm, and Luke D. Lavis (Janelia) for Janelia Fluor HaloTag ligands and Yoav Adam for providing advice on GEVI imaging. We thank Rodney Lucas for assistance performing animal experiments and Christina Steyn and Dorit Hockman for advice performing snRNAseq analysis. The research leading to these results has received support from the National Research Foundation of South Africa, a Wellcome Trust Seed Award (214042/Z/18/Z), the South African Medical Research Council, the FLAIR Fellowship Programme (FLR\R1\190829): a partnership between the African Academy of Sciences and the Royal Society funded by the UK Government's Global Challenges Research Fund, a Wellcome Trust International Intermediate Fellowship (222968/Z/21/Z), ERC Grant Agreement 617670 and the project was supported by funding from BBSRC project BB/S007938/1.

Author contributions:

Conceptualization: JSS, ASA, ERS, CJA, JVR

Tool provision: ASA, ERS

Investigation: JSS, TJSS, RJB, EFS, KMD, SEN, JVR

Writing: JSS, CJA, JVR

Supervision: JVR

Funding acquisition: CJA, JVR

Declaration of interests:

The authors declare no competing interests:

Supplemental information:

Supplementary Figure 1. *The ORCHID construct.* Voltron2-ST is expressed together with GtACR2 via a P2A linker sequence, with a Flex design and expression under the EF-1α promoter.

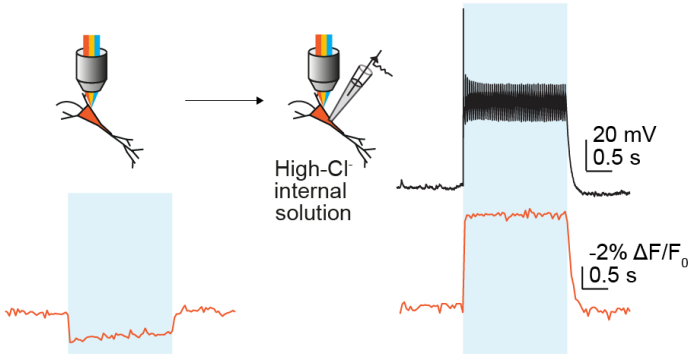

Supplementary Figure 2: *ORCHID can detect changes in DF_{Cl} induced by an increase in $[Cl^-]_i$ imposed by dialysis.* Schematic (top left) showing ORCHID used to record DF_{Cl} in a neuron at baseline (bottom left, orange trace) and again after being patched with high-Cl^- (141 mM) intracellular solution (right). Both voltage imaging (bottom right, orange trace) and current-clamp recordings (top right, black trace) showed a transition to a strongly depolarizing DF_{Cl}. Action potentials are truncated due to the low-pass behavior of the image acquisition frequency (25 Hz) and averaging of responses (see **Methods**).

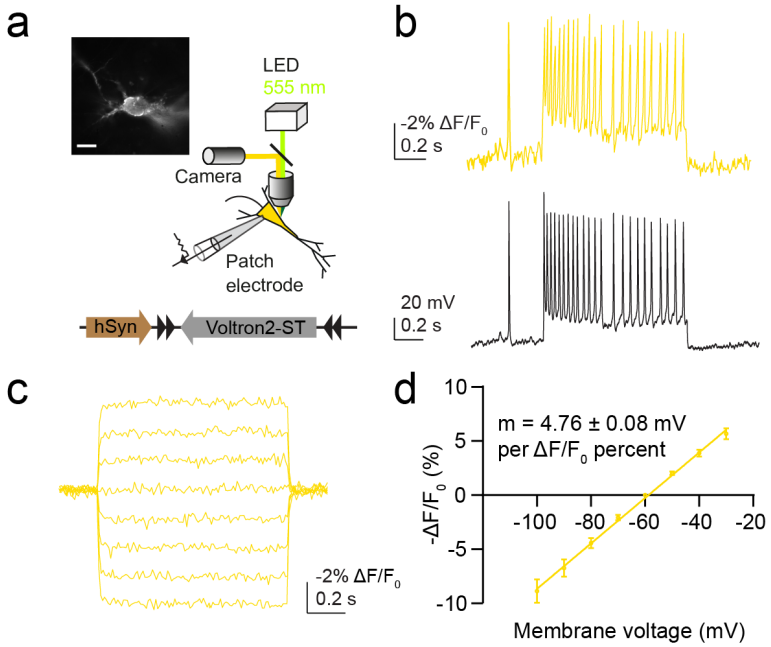

Supplementary Figure 3: *Characterizing Voltron2$_{549}$-ST for measurement of V_m.* **a**, Schematic of experimental setup for patch-clamp characterization of Voltron2$_{549}$-ST in mouse hippocampal organotypic brain slice cultures. Inset: widefield fluorescence image of the neuron patched in 'b'; scale bar: 10 µm. **b**, Current-clamp recording (black trace) and the Voltron2$_{549}$-ST fluorescence response (yellow trace) following a 200 pA current injection. **c**, Voltron2$_{549}$-ST fluorescence response to 10 mV voltage steps (V_{hold} = -60 mV). **d**, Voltage-fluorescence relation of Voltron2$_{549}$-ST, with a slope 4.76 ± 0.08 mV per $\Delta F/F_0$ percent (R^2 = 0.9236, *n* = 7).

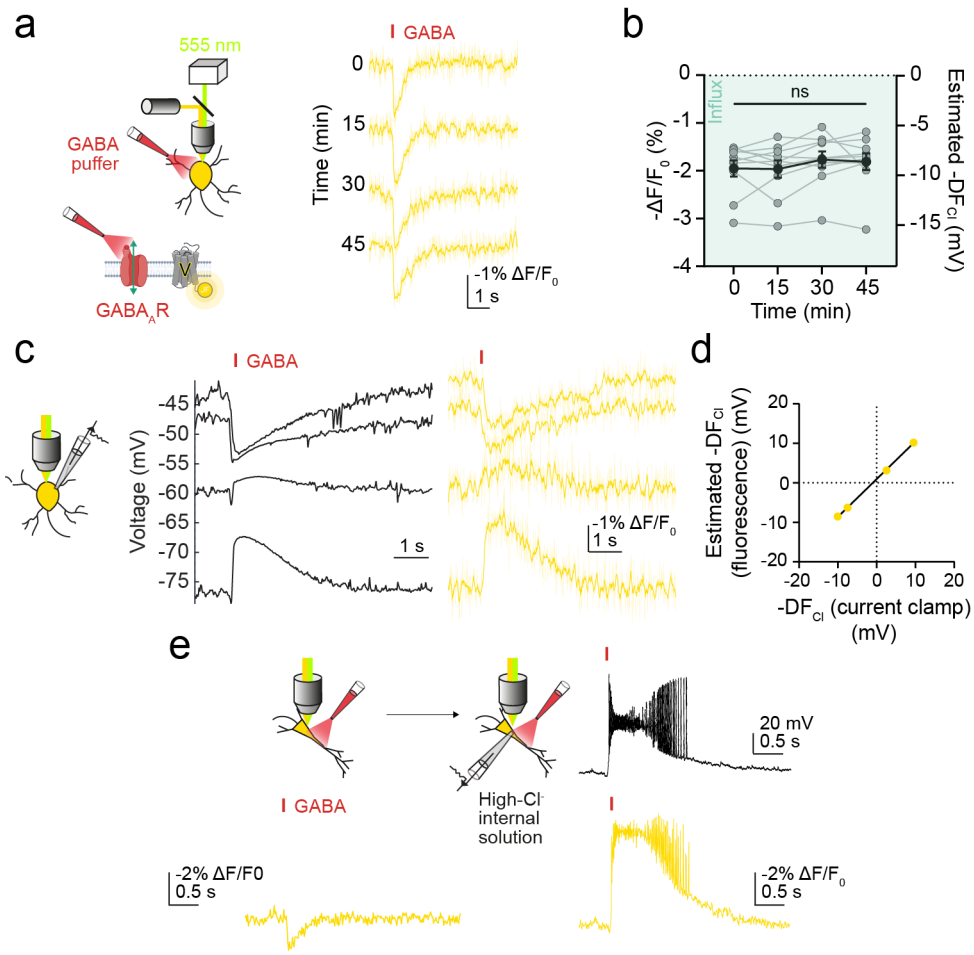

Supplementary Figure 4: *Characterizing Voltron2$_{549}$9-ST for measurement of DF$_{Cl}$ via activation of endogenous GABA$_A$Rs.* **a**, Left, schematic demonstrating imaging of Voltron2$_{549}$-ST together with activation of endogenously expressed GABA$_A$Rs through picolitre delivery of 500 μM GABA (red) directed at the cell soma, with 5 μM CGP-55845 used to block GABA$_B$Rs. Right, repeated fluorescence transients (yellow traces) in response to GABA application (red bar) recorded over 45 min. **b**, Population data showing estimates of DF$_{Cl}$ calculated from ΔF/F$_0$ remained stable (Friedman test, P = 0.2933, n = 10). Green shading indicates direction of estimated anion flux. **c**, Voltron2$_{549}$-ST and activation of GABA$_A$Rs were used to estimate DF$_{Cl}$ in neurons current-clamped at a range of V$_m$ values (left panel, V$_m$; right panel, fluorescence). **d**, The voltage-fluorescence relation of Voltron2$_{549}$-ST (**Supplementary Fig. 3d**) was used to convert ΔF/F$_0$ measurements at each V$_m$ to estimated DF$_{Cl}$ values. These were equivalent to the DF$_{Cl}$ values recorded at each V$_m$ using the current-clamp recording (R^2 = 0.9996). **e**, Schematic (top left) showing Voltron2$_{549}$-ST and activation of GABA$_A$Rs used to estimate DF$_{Cl}$ in neurons at baseline (bottom left, yellow trace) and again after being patched with high-Cl$^-$ (141 mM) intracellular solution. Both voltage imaging (bottom right, yellow trace) and current-clamp recordings (top right, black trace) showed a transition to a strongly depolarizing response to GABA$_A$R activation after Cl$^-$ loading. ns = not significant (P > 0.05); error bars indicate mean ± SEM.

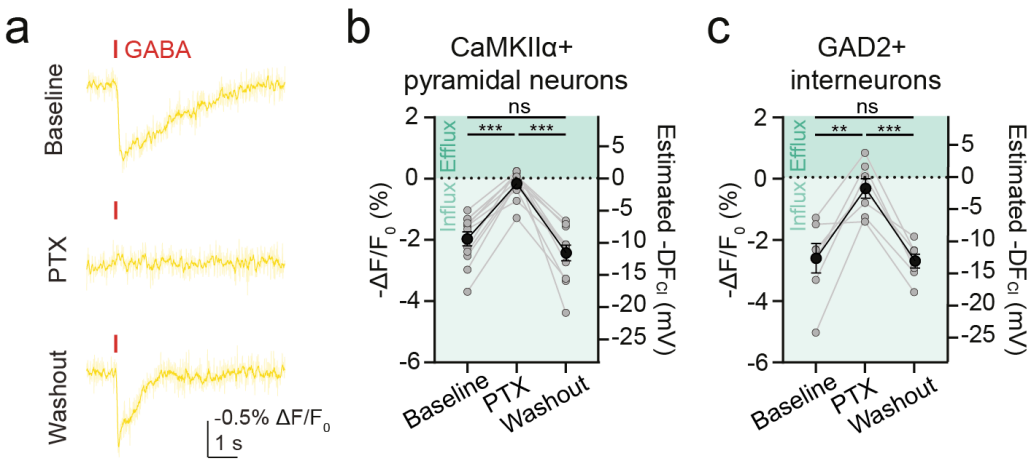

Supplementary Figure 5: *Voltron2$_{549}$-ST fluorescence estimates of DF$_{Cl}$ are mediated by GABA$_A$Rs.* **a**, Voltron2$_{549}$-ST and GABA puffs were used to record DF$_{Cl}$ in virally transfected organotypic hippocampal neurons at baseline, during picrotoxin (PTX; 100 μM) wash-in, and again after PTX washout. **b**, Population data showing recordings of DF$_{Cl}$ in CaMKIIα+ pyramidal neurons measured hyperpolarizing DF$_{Cl}$ at baseline, with this response disappearing upon PTX wash-in (Wilcoxon matched-pairs signed rank test, $P = 0.0005$, $n = 12$). The hyperpolarizing DF$_{Cl}$ response returned upon PTX washout (baseline vs washout: paired t-test, $P = 0.1256$, $n = 12$; PTX vs washout: Wilcoxon matched-pairs signed rank test, $P = 0.0005$, $n = 12$). **c**, Population data for GAD2+ interneurons (baseline vs PTX: paired t-test, $P = 0.0032$, $n = 7$; baseline vs washout: paired t-test, $P = 0.8604$, $n = 7$; PTX vs washout: paired t-test, $P = 0.0002$, $n = 7$). Green shading indicates direction of estimated Cl^- flux. ns = not significant ($P > 0.05$); $^{**}P \leq 0.01$; $^{***}P \leq 0.001$; error bars indicate mean ± SEM.

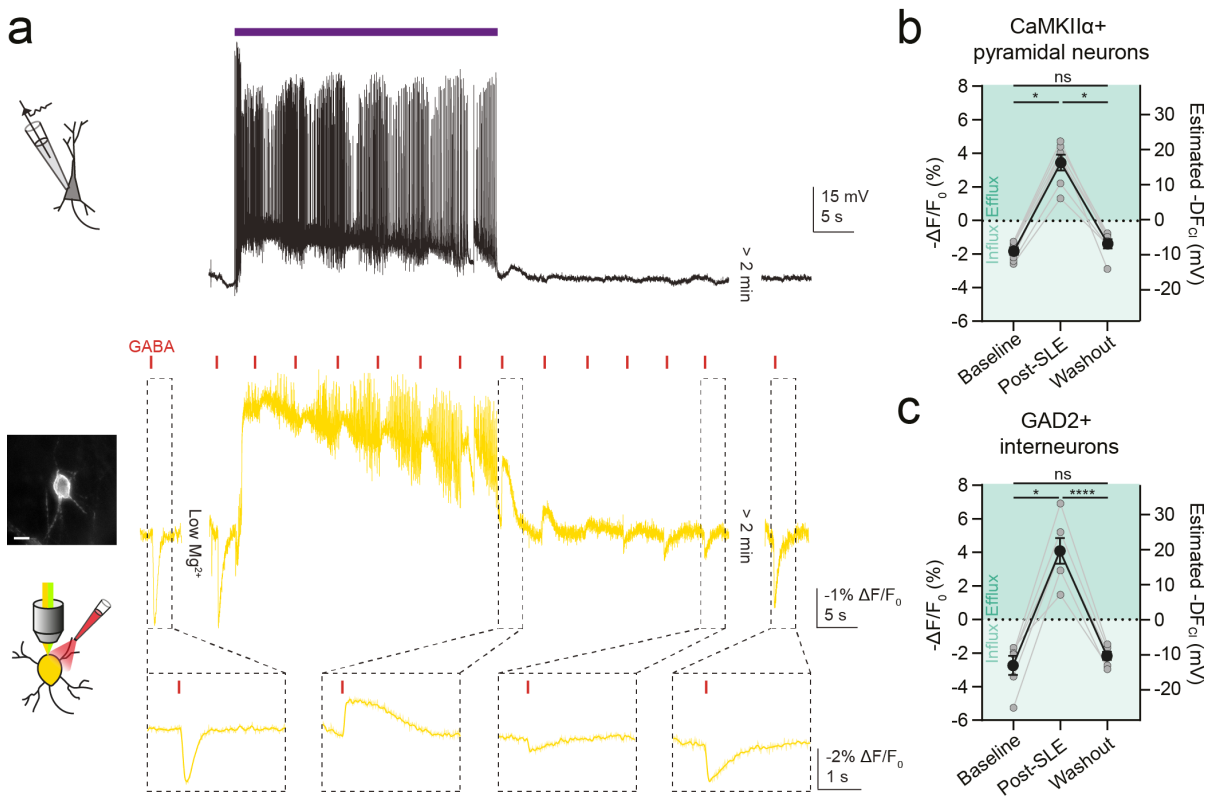

Supplementary Figure 6: *Cell-type-specific dynamics in DF_{Cl} recorded using Voltron2$_{549}$-ST and $GABA_AR$ activation during SLEs.* **a**, Voltron2$_{549}$-ST and $GABA_AR$ activation were used to investigate activity-dependent variation in DF_{Cl} in neurons in mouse hippocampal organotypic brain slice cultures. SLEs were induced using the low-Mg^{2+} model of *in vitro* SLEs. A whole-cell current-clamp recording from a CA1/3 pyramidal neuron provided an independent readout of SLEs (top panel; purple bar indicates SLE). Concurrent Voltron2$_{549}$-ST recordings were used to simultaneously record DF_{Cl} in target cells, whilst also providing a recording of the SLE (bottom panel, yellow traces). Central inset image: widefield fluorescence image of the GAD2+ interneuron from which the recording was made; scale bar: 10 µm. Baseline recordings of DF_{Cl} were made prior to low-Mg^{2+} aCSF wash-in (labelled as "Low Mg^{2+}"), immediately post-SLE (< 20 seconds after SLE cessation), and > 2 min after SLE cessation (washout). **b**, Population data of DF_{Cl} in CaMKIIα+ pyramidal neurons showed a shift from hyperpolarizing DF_{Cl} at baseline to depolarizing DF_{Cl} post-SLE (Wilcoxon matched-pairs signed rank test, $P = 0.0156$, $n = 6$). > 2 min after the SLE (washout), DF_{Cl} had returned to baseline levels (baseline vs washout: Wilcoxon matched-pairs signed rank test, $P = 0.1563$, $n = 7$; post-SLE vs washout: Wilcoxon matched-pairs signed rank test, $P = 0.0156$, $n = 7$). **c**, Similar results were recorded in GAD2+ interneurons (baseline vs post-SLE: Wilcoxon matched-pairs signed rank test, $P = 0.0313$, $n = 7$; baseline vs washout: Wilcoxon matched-pairs signed rank test, $P = 0.2188$, $n = 6$; post-SLE vs washout: paired t-test, $P < 0.0001$, $n = 6$). Green shading indicates direction of anion flux. ns = not significant ($P > 0.05$); *$P \leq 0.05$; **$P \leq 0.01$; ****$P \leq 0.0001$; error bars indicate mean ± SEM.

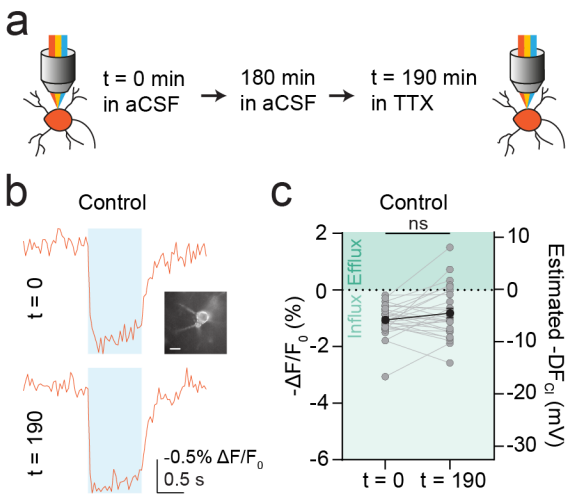

Supplementary Figure 7: *ORCHID estimates of DF_{Cl} are stable over 190 min.* **a**, Schematic of experimental design with ORCHID used to make paired recordings of DF_{Cl} 190 min apart in the same GAD2+ interneurons in organotypic hippocampal brain slices. **b**, Top, baseline recording from a GAD2+ interneuron before slice was incubated in normal aCSF for 180 min. Bottom, another recording from the same cell after the slice had been transferred to aCSF containing TTX (1 µm) for 10 min. Inset: widefield fluorescence image of recorded neuron; scale bar = 10 µm. **c**, Population data shows DF_{Cl} was not significantly different at t = 0 and t = 190 (Wilcoxon matched-pairs signed rank test, $P = 0.2297$, $n = 29$). ns = not significant ($P > 0.05$); error bars indicate mean ± SEM.